THE ICELAND GREENLAND SEAS PROJECT

I. A. Renfrew, R. S. Pickart, K. Våge, G. W. K. Moore, T. J. Bracegirdle, A. D. Elvidge, E. Jeansson, T. Lachlan-Cope, L. T. McRaven, L. Papritz, J. Reuder, H. Sodemann, A. Terpstra, S. Waterman, H. Valdimarsson, A. Weiss, M. Almansi, F. Bahr, A. Brakstad, C. Barrell, J. K. Brooke, B. J. Brooks, I. M. Brooks, M. E. Brooks, E. M. Bruvik, C. Duscha, I. Fer, H. M. Golid, M. Hallerstig, I. Hessevik, J. Huang, L. Houghton, S. Jónsson, M. Jonassen, K. Jackson, K. Kvalsund, E. W. Kolstad, K. Konstali, J. Kristiansen, R. Ladkin, P. Lin, A. Macrander, A. Mitchell, H. Olafsson, A. Pacini, C. Payne, B. Palmason, M. D. Pérez-Hernández, A. K. Peterson, G. N. Petersen, M. N. Pisareva, J. O. Pope, A. Seidl, S. Semper, D. Sergeev, S. Skjelsvik, H. Søiland, D. Smith, M. A. Spall, T. Spengler, A. Touzeau, G. Tupper, Y. Weng, K. D. Williams, X. Yang, and S. Zhou

A coordinated atmosphere–ocean research project, centered on a rare wintertime field campaign to the Iceland and Greenland Seas, seeks to determine the location and causes of dense water formation by cold-air outbreaks.

The subpolar region of the North Atlantic is crucial for the global climate system. It is where densification and sinking of ocean waters takes place, driven by strong air–sea buoyancy fluxes, constituting the headwaters of the Atlantic meridional overturning circulation (AMOC; e.g., Buckley and Marshall 2016). As such, coupled atmosphere–ocean processes, on a variety of spatial scales, require an integrated approach for their improved understanding and prediction. This region has "enhanced communication" between the atmosphere and ocean; wintertime atmospheric forcing strongly dictates ocean properties, thermal structure, and circulation. While during warm, moist, midlatitude airmass intrusions the air–sea fluxes are moderate and can even lead to ocean warming (e.g., Moore et al. 2012; Pithan et al. 2018); intermittent cold-air outbreaks (CAOs) result in large surface fluxes of heat and ▶

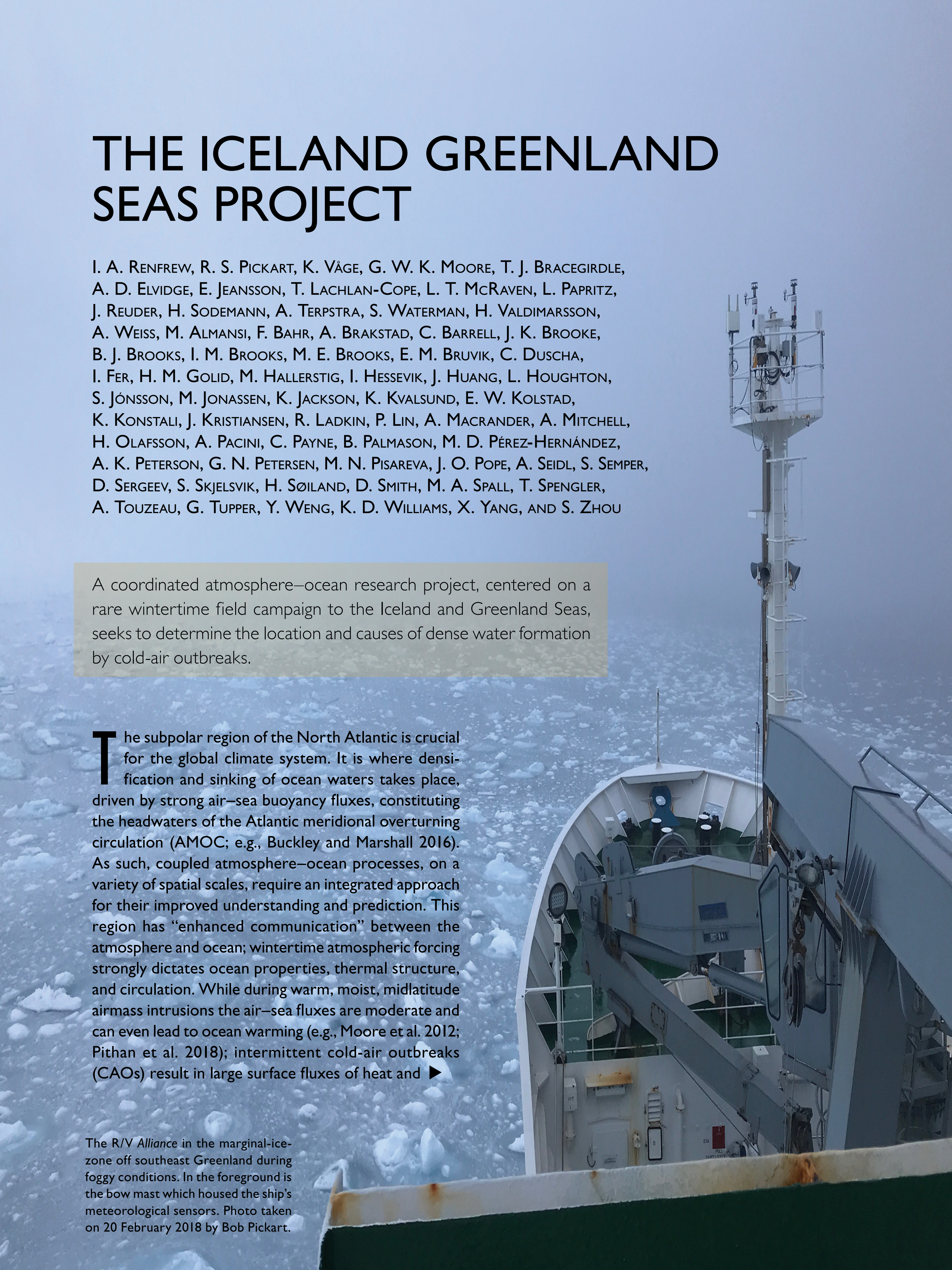

The R/V *Alliance* in the marginal-ice-zone off southeast Greenland during foggy conditions. In the foreground is the bow mast which housed the ship's meteorological sensors. Photo taken on 20 February 2018 by Bob Pickart.

moisture that make the surface waters colder, saltier, and denser. This drives convective overturning that contributes to the lower limb of the AMOC. These subpolar seas are therefore a "mixing pot" for the water masses of the North Atlantic. Previous studies suggest that the dominant contribution to the AMOC and its variability comes from the subpolar seas to the east of Greenland (Pickart and Spall 2007; Holte and Straneo 2017; Lozier et al. 2019). *However, exactly where, when, and how the water-mass transformations occur remain unclear.*

The dense water formed in the Nordic Seas (collectively the Norwegian, Greenland, and Iceland Seas) enters the North Atlantic through gaps in the submarine ridge between Greenland and Scotland (Østerhus et al. 2019). The largest amount of water flows through Denmark Strait. Debate about where the Denmark Strait Overflow Water (DSOW) originates from has been ongoing for decades. Originally, the Iceland Sea and/or the Greenland Sea was thought to be the source of the dense water via open-ocean convection to intermediate depths (e.g., Swift and Aagaard 1981; Strass et al. 1993). However, subsequently it was argued that the light-to-dense transformation takes place in the boundary current system encircling the Nordic Seas. In particular, the warm, salty water in the northward-flowing Norwegian Atlantic Current is made colder and fresher, and this dense water then returns southward in the East Greenland Current, ultimately exiting through Denmark Strait (Mauritzen 1996; see Fig. 1). While this "rim current" overturning loop is now well established, a current carrying dense overflow water toward Denmark Strait was subsequently discovered along the northern Iceland slope (Jónsson and Valdimarsson 2004). This has been dubbed the North Icelandic Jet (NIJ), and it provides the densest third of the DSOW (Harden et al. 2016). However, the process by which the NIJ is formed, and the source of the dense water it advects, remains unknown. It has been argued that the dense water is formed in the Iceland Sea or southern Greenland Sea as part of an interior overturning loop (Våge et al. 2013, 2015), but this remains a hypothesis. In terms of physical oceanography and meteorology, this region is arguably the least well studied of the North Atlantic's subpolar seas.

The broadscale climate of the Iceland Sea region is dominated by the climatological Icelandic low—the northern center of action of the North Atlantic

AFFILIATIONS: Renfrew, Elvidge, Barrell, Sergeev, Smith, and Zhou—School of Environmental Sciences, University of East Anglia, Norwich, United Kingdom; Pickart, McRaven, Bahr, Houghton, Lin, Mitchell, Pacini, Spall, and Tupper—Woods Hole Oceanographic Institution, Woods Hole, Massachusetts; Våge, Reuder, Sodemann, Brakstad, Bruvik, Duscha, Fer, Golid, Hessevik, Jackson, Konstali, Peterson, Seidl, Semper, Skjelsvik, Spengler, Touzeau, and Weng—Geophysical Institute, University of Bergen, and Bjerknes Centre for Climate Research, Bergen, Norway; Moore—Department of Physics, University of Toronto, Toronto, Ontario, Canada; Bracegirdle, Lachlan-Cope, Weiss, Ladkin, and Pope—British Antarctic Survey, Cambridge, United Kingdom; Jeansson, Hallerstig, and Kolstad—Norwegian Research Centre, Bjerknes Centre for Climate Research, Bergen, Norway; Papritz—Institute for Atmospheric and Climate Science, Department of Environmental System Science, ETH Zurich, Zurich, Switzerland; Terpstra—School of Environmental Sciences, University of East Anglia, Norwich, United Kingdom, and Geophysical Institute, University of Bergen, and Bjerknes Centre for Climate Research, Bergen, Norway; Waterman and Payne—Department of Earth, Ocean and Atmospheric Sciences, University of British Columbia, Vancouver, British Columbia, Canada; Valdimarsson, Macrander, and Pérez-Hernández—Marine and Freshwater Research Institute, Reykjavik, Iceland; Almansi—Department Earth and Planetary Sciences, The Johns Hopkins University, Baltimore, Maryland; Brooke, M. E. Brooks, and Williams—Met Office, Exeter, United Kingdom; B. J. Brooks—National Centre for Atmospheric Science, University of Leeds, Leeds, United Kingdom; I. M. Brooks—School of Earth and Environment, University of Leeds, Leeds, United Kingdom; Huang—Woods Hole Oceanographic Institution, Woods Hole, Massachusetts, and Ministry of Education Key Laboratory for Earth System Modeling, and Department of Earth System Science, Tsinghua University, Beijing, China; Jónsson—Marine and Freshwater Research Institute, Reykjavik, and University of Akureyri, Akureyri, Iceland; Jonassen—Geophysical Institute, University of Bergen, and Bjerknes Centre for Climate Research, Bergen, and Department of Arctic Geophysics, University Centre in Svalbard, Longyearbyen, Norway; Kvalsund—Runde Environmental Centre, Runde, Norway; Kristiansen—Norwegian Meteorological Institute, Oslo, Norway; Olafsson—University of Iceland, Reykjavik, Iceland; Palmason and Petersen—Icelandic Meteorological Office, Reykjavik, Iceland; Pisareva—Shirshov Institute of Oceanology, Russian Academy of Sciences, Moscow, Russia; Søiland—Institute of Marine Research, Bergen, Norway; Yang—Danish Meteorological Institute, Copenhagen, Denmark

CORRESPONDING AUTHOR: Professor Ian Renfrew, i.renfrew@uea.ac.uk

The abstract for this article can be found in this issue, following the table of contents.

DOI:10.1175/BAMS-D-18-0217.1

In final form 8 June 2019

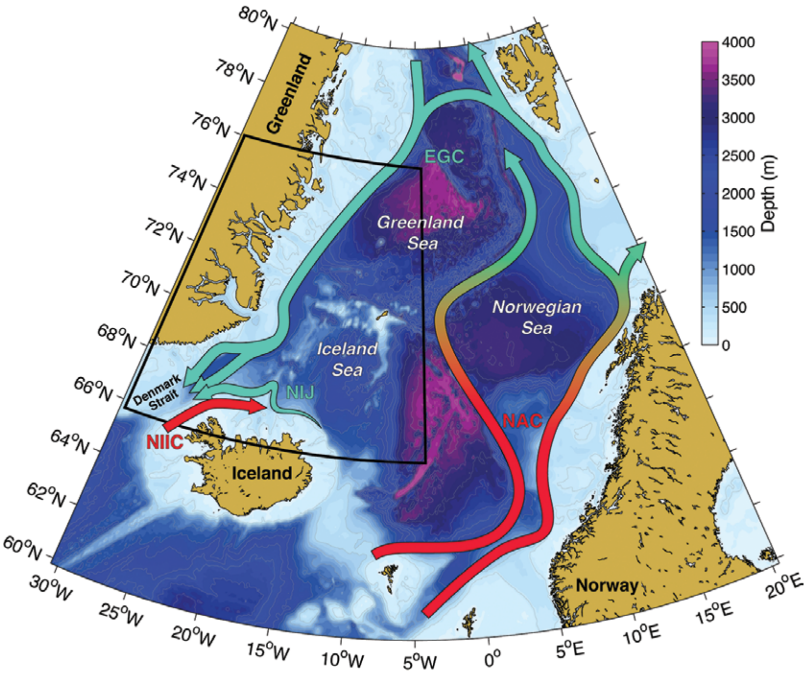

Fig. 1. Schematic of the major boundary currents of the Nordic Seas overlaid on a map of bathymetry (shading). The subtropical origin water entering the Norwegian Sea gradually cools and becomes denser as it circulates around the perimeter of the basins, exiting as overflow water through the west side of the Denmark Strait. The warm water entering Denmark Strait is believed to be converted into the overflow water flowing southward through the east side of the strait. The IGP study area is delimited by the black lines. Abbreviations are NAC = Norwegian Atlantic Current, EGC = East Greenland Current, NIIC = North Icelandic Irminger Current, NIJ = north Icelandic jet.

Oscillation (NAO). When this climatological low is deep (NAO+), extratropical cyclones bring relatively warm maritime air from the south and east over the Iceland Sea. When it is shallow (NAO−), other synoptic-scale weather regimes dominate; for example, a deep Lofoten low can bring cold polar air from the north over the Greenland and Iceland Seas (e.g., Jahnke-Bornemann and Brümmer 2008), while a northeasterly displaced Icelandic low can force barrier winds off eastern Greenland over the Iceland Sea (e.g., Harden et al. 2011). The interplay between the NAO and other climate modes—such as the east Atlantic and Scandinavian patterns—has a profound impact on the atmospheric circulation of the subpolar North Atlantic and the associated forcing of the ocean (e.g., Cassou et al. 2004). Compared to the rest of the subpolar North Atlantic, the wintertime surface turbulent heat fluxes over the Iceland Sea have a local minimum (Moore et al. 2012). This is the result of a balance between low heat flux events (warm air from the south) and high heat flux events (CAOs from the north). Harden et al. (2015) illustrate this synoptically driven episodic nature using rare meteorological buoy observations from the central Iceland Sea. They show that CAOs with surface turbulent heat fluxes of ~200 W m^{-2} typically last 2–4 days and occur every 1–2 weeks. It is these CAOs that are responsible for the majority of the high heat flux events in the western Nordic Seas, with the amount of oceanic heat loss governed by airmass pathways, location, surface conditions, and the meteorological environment (e.g., Papritz and Spengler 2017; Brümmer 1997).

Although the broadscale atmosphere–ocean coupling is dictated by synoptic-scale variability, there are a myriad of mesoscale weather features—including orographic jets, ice-edge jets, Arctic fronts, and polar mesoscale cyclones—that are much more challenging to characterize, simulate, and predict (e.g., Vihma et al. 2014). These mesoscale features can have a significant impact on the ocean; for example, increasing the mixed layer depth in the subpolar North Atlantic and the amount of DSOW transported south when accounted for in ocean models (Condron and Renfrew 2013; Jung et al. 2014). This highlights the requirement of resolving the atmospheric forcing on both synoptic scales and mesoscales. Current numerical weather prediction (NWP) models, and some high-resolution climate simulations, can potentially provide accurate atmospheric forcing, but there are a variety of concerns about their quality. For example, air–sea–ice interactions over sea ice—particularly over the marginal ice zone (MIZ)—are difficult to observe and are often crudely represented in models. Biases in surface fluxes over the MIZ can be substantial and extend hundreds of kilometers downstream (e.g., Bourassa et al. 2013). Such biases are caused by poor representation of surface exchange (e.g., unrepresentative drag coefficients; see Elvidge et al. 2016; Renfrew et al. 2019) or inadequate atmospheric boundary layer parameterizations (e.g., Renfrew et al. 2009; Boutle et al. 2014; de Roode et al. 2019). Consequently, even though the broadscale meteorology can be reasonably well simulated, the associated air–sea interaction can be difficult to capture accurately, particularly during CAOs over the MIZ.

The Iceland and Greenland Seas are also experiencing profound changes related to anthropogenic climate change. The dramatic retreat of summer sea ice over the high Arctic is well known, and its causes and impacts are active areas of research. By contrast, relatively little attention has been paid to the equally dramatic retreat of winter sea ice: a 10% decade^{-1} decline in extent for a region encompassing the Greenland, Iceland, and Irminger Seas (Parkinson and Cavalieri 2008). Moore et al. (2015) show that this wintertime retreat is influencing the climatological pattern of surface heat fluxes over these seas, leading to a significant negative trend in heat fluxes over both the central Iceland and Greenland Seas. This in turn implies a change in the properties and volume of dense water created in these locations. The retreat can also lead to water-mass transformation in areas along the Greenland continental slope that were previously insulated from the atmosphere underneath sea ice, perhaps even directly into the East Greenland Current (Våge et al. 2018). It is argued that changes in water-mass modification appear to be one of the contributing factors to an exceptional slowdown in the overturning of the AMOC in recent years (Rahmstorf et al. 2015; Caesar et al. 2018), although there is no evidence that the dense water overflowing from the Nordic Seas has weakened (Østerhus et al. 2019). This is broadly consistent with Sévellec et al. (2017), who argue that changes in surface fluxes in the subpolar North Atlantic have the greatest impact on the AMOC over decadal time scales, while changes in the Nordic Seas and Arctic Ocean have the greatest impact over multidecadal time scales, driven by a reduced sea ice pack. Additional processes, such as increased runoff from the glacial melt of Greenland (Böning et al. 2016) or changes in the characteristics of the Atlantic water entering the Nordic Seas region (Glessmer et al. 2014), are also likely to be critical. In short, profound changes in the way the atmosphere and ocean interact in this region are underway, yet we do not understand their consequences largely because we do not know how the present system works.

The Iceland Greenland Seas Project (IGP) has been developed in response to some of these uncertainties in the North Atlantic climate system. It focuses on the atmosphere–ocean coupling, air–sea–ice interaction, and the resulting impacts on the atmospheric and oceanic characteristics and circulation. The overarching hypothesis for the IGP is that *wintertime convection in the northwest Iceland Sea and southwest Greenland Sea, forced by intermittent cold-air outbreaks, forms the densest component of the AMOC.*

The IGP is endorsed by the World Meteorological Organization's decade-long Polar Prediction Project with a focus on the Year of Polar Prediction (YOPP) from 2017 to 2019 (Jung et al. 2016; see www.polarprediction.net). Our project contributes toward the overarching YOPP aims by providing observations and insights on processes that are necessary to improve environmental forecasts from days to seasons, which are presently far less skillful for the polar regions than the midlatitudes.

A novelty of the IGP has been to develop and execute our research *entirely within a coupled atmosphere–ocean framework*. This coupled framework has guided the development of our scientific hypothesis and objectives, our securing of funding from different international agencies, our field campaign planning and execution, and our observational analysis and numerical modeling experiments. At times this has been testing! Wintertime field work in the subpolar seas brings a host of challenges, and coordinating a research vessel and research aircraft added another. But our approach has brought many benefits too, including a deeper understanding of the coupled system. Indeed, it is envisioned that our joint observational datasets will lead to a number of important steps forward, as we preview in the remainder of this article.

THE WINTERTIME CRUISE. In February–March 2018, we carried out a 43-day cruise on the NATO Research Vessel *Alliance* consisting of two legs in the northwest Iceland Sea and southwest Greenland Sea. Our main objectives were to 1) document the ventilation of dense water in the region; 2) characterize the ocean's and atmosphere's response to CAOs downwind of the ice edge; 3) determine the exchange of newly ventilated dense water between the Greenland and Iceland Seas; 4) elucidate the dynamics and time scales that link the ventilation process, the circulation and mixing of the newly formed water, and the manner in which the dense water feeds the NIJ; and 5) continuously characterize the structure of the atmospheric boundary layer (ABL).

Our shipboard oceanographic instrumentation included a conductivity–temperature–depth (CTD) system attached to a rosette with twelve 5-L Niskin bottles for sampling salinity, dissolved oxygen, nutrients, the transient tracers CFC-12 and SF_6, and the stable water isotopologues $H_2{}^{18}O$ and HDO. We used expendable CTDs (XCTDs) and bathythermographs (XBTs) in inclement weather and to increase the spatial resolution. We made velocity measurements using two hull-mounted acoustic

Doppler current profilers (a 150-kHz unit and a 75-kHz unit), and sampled sea surface conditions continuously via an underway CTD. A summary is given in Table 1. The *Alliance*'s "Inside CTD" was deployed—hands free—from a small, heated hanger on the starboard side of the ship; this was essential due to the subfreezing air temperatures and high sea state experienced. It allowed us to carry out CTD casts in sustained 30–35 kt (1 kt ≈ 0.5144 m s^{-1}) winds.

The *Alliance* departed Reykjavik, Iceland, on 6 February for leg I of the cruise, which focused on the northwest Iceland Sea (Fig. 2). This leg can be characterized as the "section phase" of the cruise: we carried out six transects with the CTD package, or with XCTDs if the sea state or timing demanded. Most of the CTD casts reached the bottom, the exception being in the Iceland Sea gyre. Three of the sections extended into the East Greenland Current. Leg I operations ended on 21 February in Ísafjörður, Iceland.

Leg II began on 26 February 2018 and can be characterized as the "survey phase" of the cruise, with the sampling closely coordinated with the research aircraft. Shortly after leaving port a CAO developed in the Iceland Sea, and over the next week we worked in concert with the aircraft to sample the different stages of this event. After a pre-CAO XCTD survey, we began repeat occupations of two triangles in the northwest Iceland Sea (see Fig. 2b) to document the water column response to the enhanced surface heat fluxes. One aim was to calculate both ocean and atmospheric heat budgets in order to better quantify the coupled evolution of this event. We also began occupying a "time series station," which we visited seven times over the cruise. During the last phase of leg II, we steamed to the southwest Greenland Sea and occupied sections 7–10, including an excursion into the central part of the Greenland Sea gyre (Fig. 2a). By this point the ship had become more comfortable working in the MIZ, and, consequently, we sampled well into the East Greenland Current on these sections. During our steam back south, a final CTD transect (the so-called Látrabjarg Line; section 12 in Fig. 2a) was occupied to capture the structure of the overflow water passing through Denmark Strait. The cruise ended on 22 March when the *Alliance* docked in Reykjavik.

We designed the atmospheric observing program on the *Alliance* cruise to focus on the thermodynamic structure of the ABL; see Table 1 for a summary of instrumentation. During the 43 days at sea we released 100 radiosondes, with all sounding data uploaded to the Global Telecommunication System (GTS) and so available for operational forecasting. Our strategy was

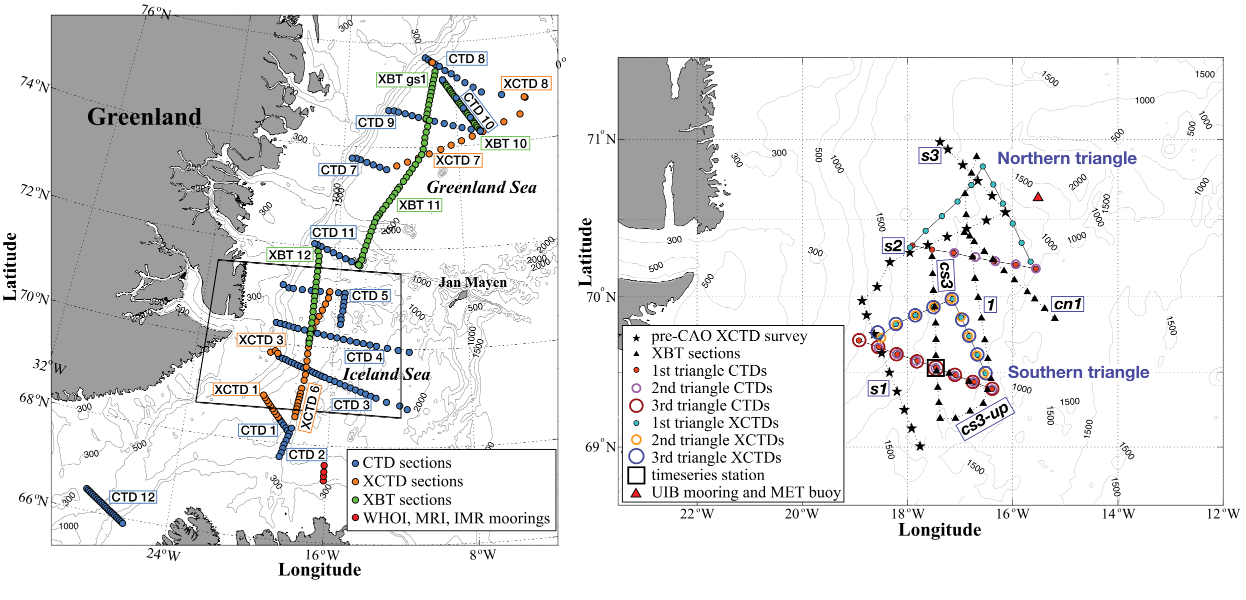

FIG. 2. Locations of the oceanographic observations from the winter 2018 cruise and the mooring deployments. (left) The hydrographic sections occupied in the Iceland and Greenland Seas; see the legend for the type of instrument used for each of the lines. The locations of the four moorings deployed across the NIJ north of Iceland are also shown. The gray contours are the isobaths. See text for acronyms. (right) The northwest Iceland Sea and the location of intensive surveys where triangular patterns or lines were repeated several times in coordination with the research aircraft; see the legend for details. The southern triangle was sampled three times using a combination of CTDs and XCTDs, while the northern triangle was sampled once. The time series CTD station was occupied seven times during the cruise. The location of the mooring and met buoy deployed in the northern Iceland Sea is also marked.

to release one sounding a day by default and more frequent soundings (up to 3-hourly) during periods of "interesting" weather or in coordination with research aircraft flights. The radiosonde observations covered the Iceland and Greenland Seas region, filling a gap in the operational observing network (Fig. 3). To provide a continuous characterization of the ABL we deployed a HatPro radiometer (e.g., Tjernström et al. 2019) sitting on a motion-correction platform (following Achtert et al. 2015) and a Windcube Doppler lidar which has an inbuilt motion-correction algorithm (e.g., see Kumer et al. 2016). The profiling instruments were configured

Table 1. A summary of the IGP observing system. Variables measured are T = temperature; S = salinity; p = pressure; O_2 = oxygen; u, v, w = velocities; SST = sea surface temperature; CFC = chlorofluorocarbons; SF_6 = sulfur hexafluoride; RH = relative humidity; LWP = liquid water path; PPN = precipitation; LWC = liquid water content; T_{dew} = dewpoint temperature; SW = shortwave radiation; LW = longwave radiation; q = specific humidity. Instruments marked with an asterisk had data broadcast via satellite and hence were available for operational forecasting.

Platform	Instruments	Variables	PI
Ocean observations			
R/V *Alliance*	CTD, XCTD, XBT,	T, S, p (O_2 CTD only)	R. Pickart, WHOI
	Vessel-mounted ADCP systems	u, v	R. Pickart, WHOI
	Water intake	SST	R. Pickart, WHOI
	Water sampling—geochemical tracers and isotopes	Nutrients, O_2, CFCs, and SF_6	E. Jeansson, NORCE
		$H_2{}^{18}O$, HDO	H. Sodemann, UiB
	Microstructure glider	Turbulence	S. Waterman, UBC
	Argo floats	T, S, p, u, and v (from drift)	K. Våge, UiB
Mooring	CTD, T recorder, ADCP, RCM	T, S, p, u, v	K. Våge, UiB
Seagliders	CTD, oxygen	T, S, p, O_2, u, and v (from drift)	K. Våge, UiB
Atmospheric observations			
R/V *Alliance*	Wavepak Vessel-mounted meteorology	T, p, RH, u, v,	I. Renfrew, UEA
	Vaisala MW41 Radiosonde system*	T, p, RH, u, v	I. Renfrew, UEA
	HatPro radiometer	T, RH, LWP	I. Renfrew, UEA
	+ Motion correction platform	+ motion	I. Brooks, ULeeds
	Leosphere Windcube lidar	u, v, w, turbulence	J. Reuder, UiB
	Metek Micro Rain Radar	PPN rate, LWC	H. Sodemann, UiB
	Picarro L2130-i Isotope Spectrometer	$H_2{}^{18}O$, HDO of water vapor	H. Sodemann, UiB
	Precipitation sampling	$H_2{}^{18}O$, HDO	H. Sodemann, UiB
DH6 Twin Otter	Aircraft-mounted meteorology	T, p, T_{dew}, T_{sfc}, SW, LW	T. Lachlan-Cope, BAS and I. Renfrew, UEA
	BAT turbulence probe and LICOR	u, v, w, T, q, turbulent fluxes	T. Lachlan-Cope, BAS and I. Renfrew, UEA
	DMT Cloud, Aerosol and PPN Spectrometer	Aerosol and PPN spectra, LWC	T. Lachlan-Cope, BAS and I. Renfrew, UEA
	Grimm spectrometer	Aerosol spectra	T. Lachlan-Cope, BAS and I. Renfrew, UEA
	Picarro L2130-i Isotope Spectrometer	$H_2{}^{18}O$, HDO of water vapor	H. Sodemann, UiB
Meteorological buoy	Seawatch Wavescan Buoy*	T, RH, u, v, SST, SW, ocean currents	J. Reuder and E. Kolstad, UiB

to focus on the ABL and record profiles approximately every 10 min. The radiometer, its motion-correction platform, and the wind lidar all generally performed well, yielding near-continuous datasets. We also deployed a METEK GmbH vertically pointing Micro Rain Radar (MRR-2). All of this instrumentation was located on the boat deck (one level up from the fantail). In addition, we had standard meteorological observations ~15 m above sea level on the bow mast. Unfortunately, a new anemometer that was installed prior to the cruise did not function properly and hence the wind data are of lower quality for leg I of the cruise; the anemometer was replaced for leg II.

Figure 4 shows a time series of wind speed from the *Alliance* with measurements from the ship's bow-mast anemometer, the wind lidar, and radiosonde profiles. The period illustrated, from 28 February to 2 March 2018, shows the dramatic increase in wind speed associated with the start of a long-lived CAO. Winds increased from 2 to 20 m s^{-1} in less than 12 h. The various wind speed measurements generally match and show the expected increase of wind speed with altitude. The exceptions are some 50-m radiosonde measurements, which appear to underrecord just after release (the balloons were sometimes caught in turbulence around the ship), and a period when the ship's anemometer was sheltered by the ship's superstructure. This long-lived CAO was comprehensively sampled during the campaign and is illustrated throughout this article.

Water vapor isotopes can provide information about the evaporative conditions at the ocean surface and thus pinpoint the origin of water vapor in air parcels. We sampled the isotope composition of water vapor continuously during leg II of the cruise using a Picarro L2140i with a heated inlet system. In addition, we performed isotope analysis of precipitation samples, of water column samples from the CTD

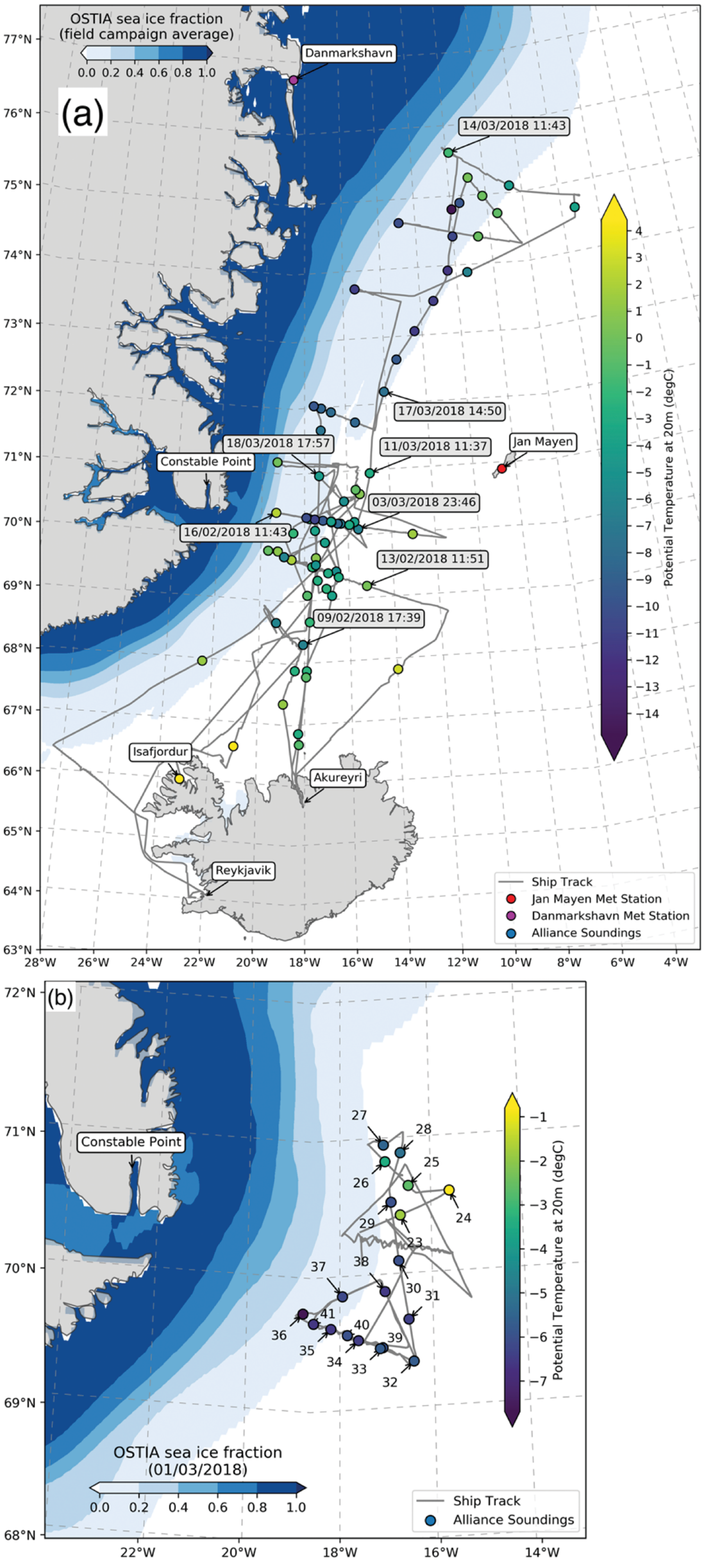

Fig. 3. Locations of radiosonde profiles from the *Alliance* cruise and relevant land stations. The *Alliance* radiosonde locations are shaded by low-level potential temperature and the cruise track is shown in gray. (a) The locations of soundings 1–22 (4–27 Feb) and 42–94 (2–18 Mar) and (b) a close-up of the locations of soundings 23–41 (28 Feb–2 Mar). The average sea ice fractions are contoured, based on the Met Office's Operational Sea Surface Temperature and Sea Ice Analysis (OSTIA) dataset.

rosette, and on 10 of the research flights. A precipitation sampling program along transects near Akureyri, in northern Iceland, further supplemented the IGP water isotope sampling and will provide unique insight into the water turnover, in particular, the evaporation sources of a CAO's water cycle (Papritz and Sodemann 2018). The water isotope measurements provide key information on mass fluxes in the

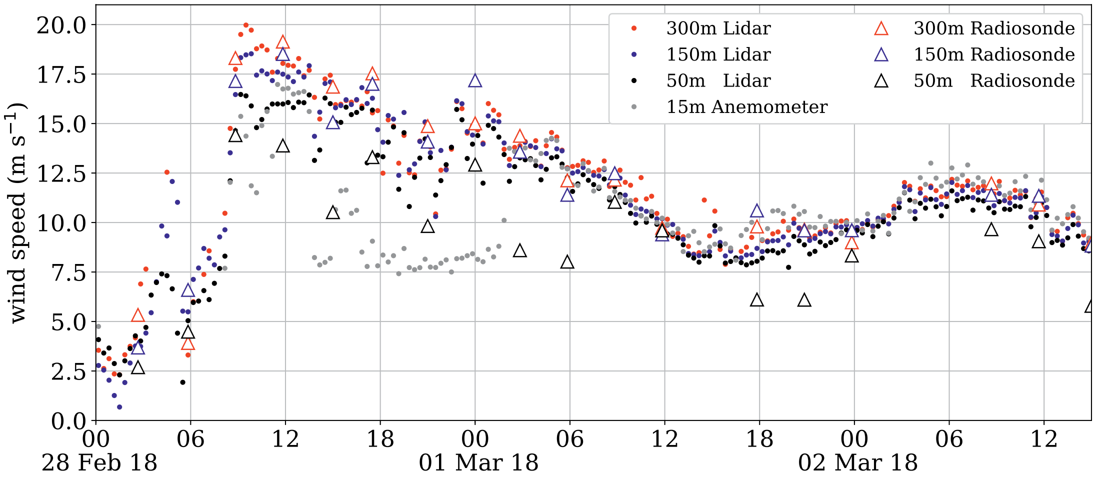

FIG. 4. Wind speed, from 28 Feb to 2 Mar 2018, from on board the *Alliance*. Measurements are from the ship's bow-mast anemometer located approximately 15 m above the sea surface, and from the Wind Cube lidar and radiosonde profiles at 50, 150, and 300 m altitude (see legend). The bow-mast anemometer was sheltered by the ship's superstructure when sailing directly downwind, hence it underestimated wind speeds from about 1400 UTC 28 Feb to 0200 UTC 1 Mar.

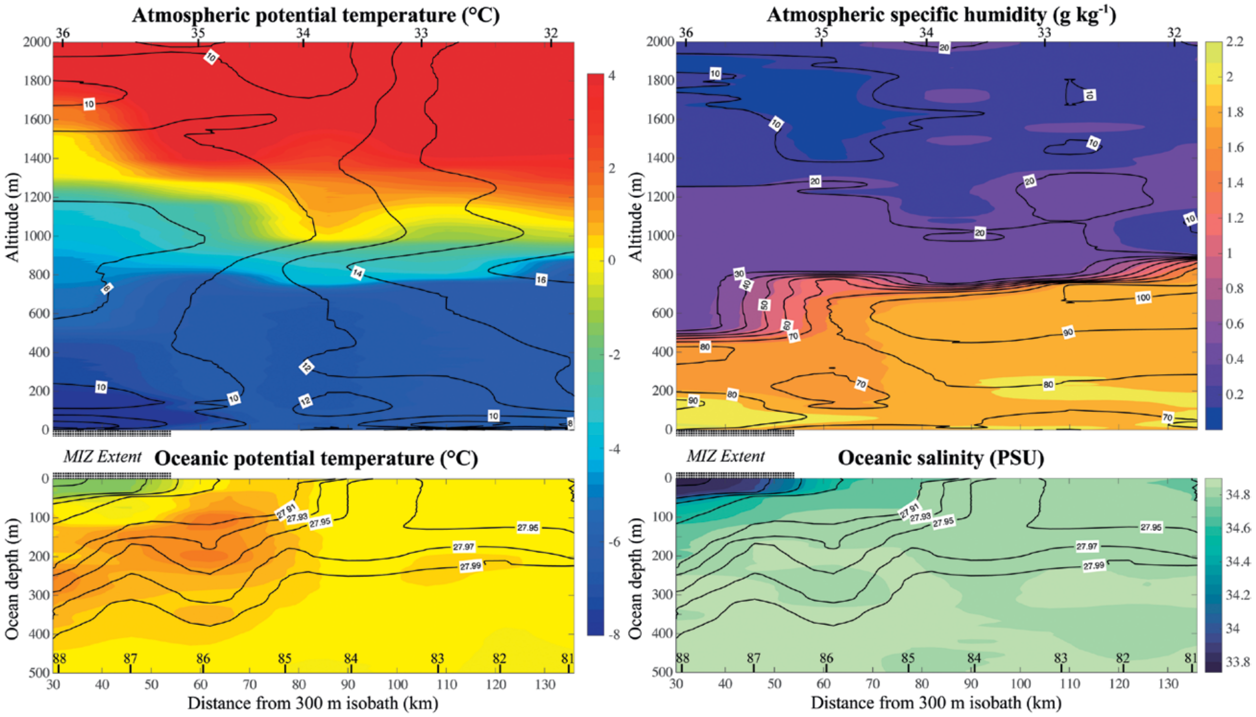

FIG. 5. A simultaneous cross section of the atmosphere and ocean on 1 Mar 2018. (top panels) Atmospheric observations from radiosonde releases (soundings 32–36); (bottom panels) oceanographic observations from CTD profiles (casts 81–88). (left) Potential temperature on a common scale (shading), overlain by contours of (top) wind speed and (bottom) potential density. (right) Specific humidity (shading) overlain by relative humidity contours for the atmosphere, and salinity (shading) overlain by potential density contours for the ocean. The contour intervals are 2 m s^{-1}, 0.02 kg m^{-3}, and 10% for wind speed, potential density, and relative humidity, respectively. The section is approximately west to east; its location is marked on Fig. 7.

coupled ocean–atmosphere system, which we will use to validate the water cycle in isotope-enabled weather prediction and climate models (e.g., following Sodemann et al. 2017).

Science operations on the *Alliance* were carried out 24 h a day. Each afternoon at 1245 UTC we held a science briefing to discuss upcoming plans, address any problems, and review the data being collected to help guide our sampling strategies. In total we occupied 189 CTD stations (152 of them with chemical sampling, 29 with water isotopes), 120 XCTDs, and 144 XBTs. This resulted in 453 profiles of the ocean mixed layer. We released 100 radiosondes and obtained near-continuous temperature and wind profiles of the atmospheric boundary layer. In short, we collected a wealth of data during a harsh wintertime period where there is a dearth of historical measurements.

Figure 5 illustrates the coupled sampling of the atmosphere and ocean that we managed from the *Alliance*, showing cross sections of the atmosphere and ocean across the east Greenland continental slope (see Figs. 2b, 3b for location), on the first day of the CAO. It shows a moderately cold, well-mixed ABL, with a near-constant potential temperature (θ) and a height of ~800 m delineated by the strong vertical θ gradient. Winds increase from west to east from about 8 to 14 m s^{-1} and are from the north to north-northwest, so approximately perpendicular to the cross section. The specific humidity is relatively high within the ABL, with a slight increase to the east where the relative humidity reaches 100% at the top of the ABL. This is consistent with the shallow convective clouds seen in satellite images from this day (e.g., Fig. 7). The underlying ocean is significantly warmer than the ABL, and hence is losing heat and moisture via surface sensible and latent heat fluxes. The location of the MIZ is marked in the figure and is evident from the lower potential temperatures of the air and ocean, and the fresher surface layer of the ocean. The isopycnals indicate some mixed layers of near-constant density, but these are relatively shallow (~100 m) so do not suggest much dense water-mass formation at this time.

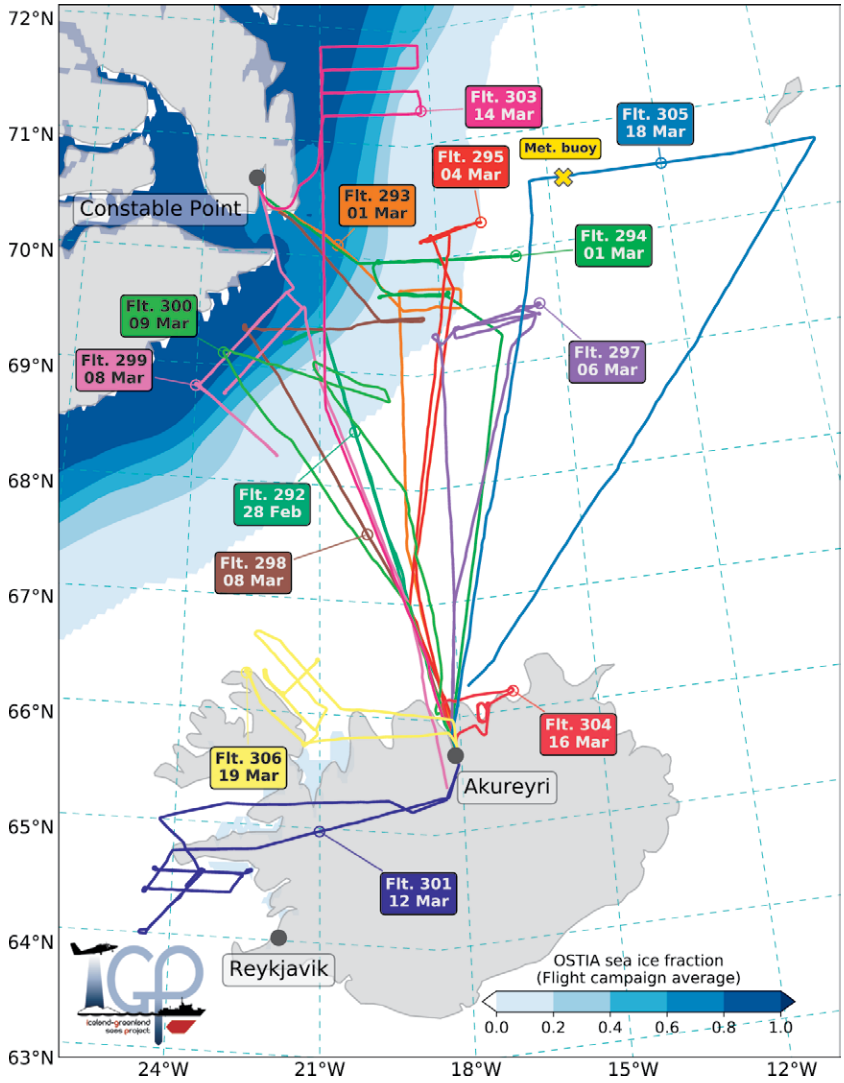

FIG. 6. Location of all science flights during the aircraft campaign. The average sea ice fraction from the period is contoured (based on OSTIA data). Flights 293, 294, 295, and 297 were in the vicinity of the *Alliance*, while flight 305 passed the meteorological buoy.

THE WINTERTIME AIRCRAFT CAMPAIGN.

The main platform for our atmospheric measurement program was the British Antarctic Survey's instrumented DH6 Twin Otter research aircraft. This is a relatively small aircraft, with an operations team of just a few people, making it cost effective and flexible with regard to operations and airports. It was fitted with an internal fuel tank that gave it an extended range to nearly 800 n mi (1 n mi = 1.852 km) or 6 h. The instrumentation is summarized in Table 1 and described in more detail in, for example, King et al. (2008) and Fiedler et al. (2010). We had 70 flight hours for the aircraft campaign and flew 14 science missions, mostly over the Iceland Sea and the MIZ off

Table 2. Campaign summary focusing on the meteorological deployments of the research aircraft and key periods of radiosonde launches from the *Alliance*. Flight comments note the number of cross sections in the ABL, determined from sawtooths between the surface and typically 1,500 m, and the amount of time flying in the surface layer (SL), typically 15–50 m, or in the ABL, typically 50–2,000 m. Text is color coded by science aim: cold-air outbreak development and structure (dark blue), surface fluxes over sea ice (cyan), turbulent structures in orographic flows (purple), and isotope composition (red). Days when the aircraft and ship tracks coincided are shaded light orange. Flight patterns are shown in Fig. 6 and radiosonde locations in Fig. 3.

Date and time (UTC)	Flight No.	Flight comments	*Alliance* radiosonde times (UTC)	Science aims
28 Feb 2018 0748–1151	292	Six short ABL cross sections; *low-level flying hampered by cloud*	0000, 0300, 0600, 0900, 1200, 1500, 1800, 2100	Cold-air outbreak onset over the Iceland Sea
1 Mar 2018 0813–1145 1306–1802	293 294	Two long ABL cross sections; 60 min (SL) and 60 min (ABL)	0000, 0300, 0600, 0900, 1200, 1500, 1800, 2100	Cold-air outbreak development and structure
2 Mar 2018			0000, 0600, 0900, 1200, 1500,	Cold-air outbreak structure
3 Mar 2018			0000, 1200	
4 Mar 2018 1016–1509	295	Two short ABL cross sections; 20 min (SL) and 40 min (ABL)	0000, 0600, 0900, 1200, 1500, 1800	Cold-air outbreak structure
5 Mar 2018 *1030–1120*	*296*	*Transit from Reykjavik to Akureyri*	0600, 0900, 1200, 1800	
6 Mar 2018 0847–1414	297	One long/one short ABL cross sections; 20 min (SL) and 40 min (ABL)	0000, 0600, 0900, 1200, 1500, 1800	Cold-air outbreak structure
8 Mar 2018 0821–1156 1327–1901	298 299	Three long ABL cross sections; 135 min (SL)		Surface fluxes over sea ice and katabatic flow structure
9 Mar 2018 0958–1447	300	One long/two short ABL cross sections; *low-level flying hampered by cloud*		Boundary layer structure over sea ice
12 Mar 2018 1213–1813	301	50 min (SL) and 85 min (ABL) flying downstream and over a mountainous ridge	0000, 1200	Orographic flow structures: lee-side fluxes, waves and wakes
14 Mar 2018 *data lost* 1255–1828	*302* 303	*Most data lost due to file error* One long ABL cross section; 100 min (SL)	0000, 1200	Surface fluxes over sea ice
16 Mar 2018 0955–1145	304	Racetrack patterns at various heights in the ABL	0000, 1200, 1500, 1800, 2100	Isotope composition survey and instrument calibration Cold-air outbreak onset over the Greenland Sea
17 Mar 2018			0000, 0300, 0600, 0900, 1200, 1500, 1800	Cold-air outbreak development
18 Mar 2018 0909–1459	305	Two short ABL cross sections; 80 min (SL) including past the meteorological buoy	0000, 0600, 0900, 1200, 1500, 1800	Cold-air outbreak structure
19 Mar 2018 1301–1729	306	Two long ABL cross sections; 20 min (SL) and 100 min (ABL)	0000, 1200	Orographic flow structures: lee-side fluxes, waves, and wakes

southeast Greenland (see Fig. 6). We were based out of Akureyri, Iceland, but also refuelled three times at Constable Point (Nerlerit Inaat), Greenland, enabling us to fly two missions on those days.

The primary science objective for the meteorological campaign was to characterize the structure and development of CAOs—focusing on surface fluxes and the ABL—especially over and downstream of sea ice. By combining the aircraft and *Alliance*-based observations, we aimed for a unique and comprehensive sampling of the marine ABL during CAOs. Two secondary science objectives were to characterize the ABL structure of orographic flows and to quantify variations in water vapor isotopes in the lower troposphere. Table 2 provides a summary of the meteorological field campaign, listing all the research flights as well as key periods of radiosonde releases from the *Alliance*; it is color coded by science objective. The Twin Otter is ideally suited for measuring the turbulent and thermodynamic structure of the ABL. Missions were planned to focus on straight and level legs in the surface layer (typically 20–50 m above the sea surface), or in the ABL (between 50 and 1,500 m), or via "sawtooth" legs ascending or descending through the depth of the ABL.

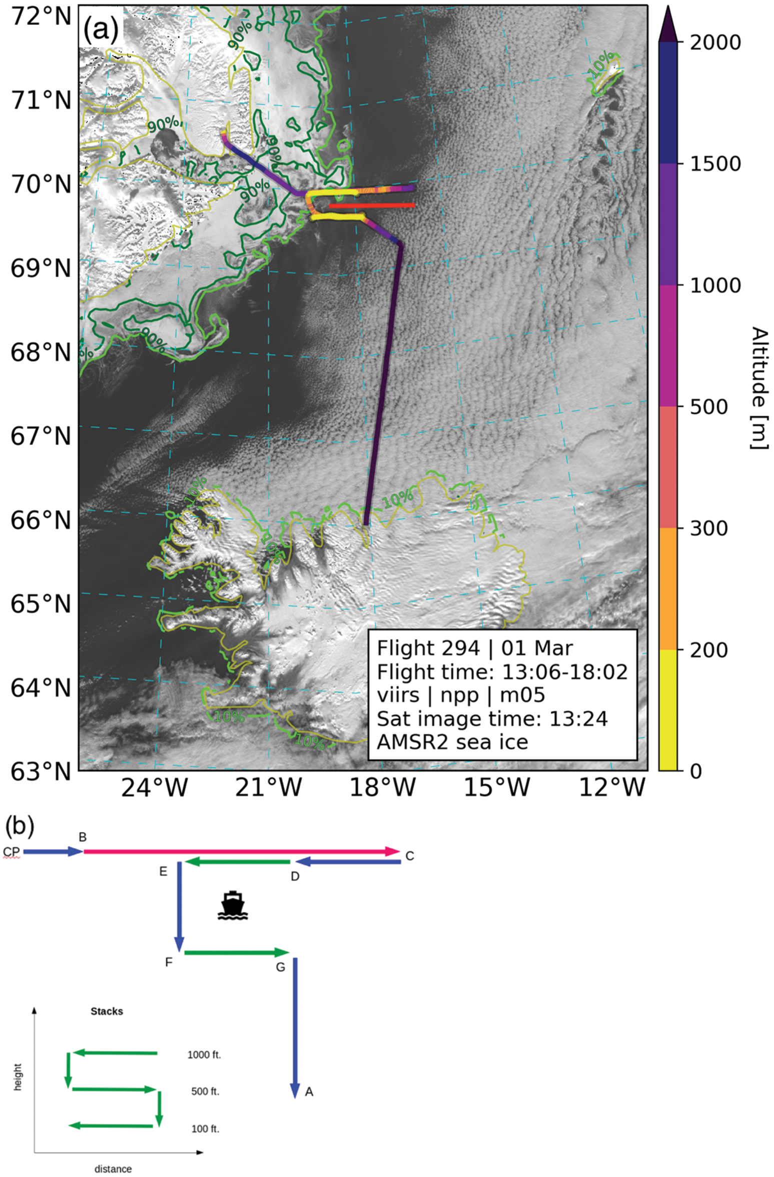

Fig. 7. (a) Aircraft track from flight 294 with aircraft altitude shaded over a VIIRS visible satellite image from 1324 UTC 1 Mar 2018. The location of the *Alliance* cross sections (Fig. 5) is shown in red. Sea ice concentration contours at 90% and 10% (dark and light green) from AMSR2 are shown (Spreen et al. 2008). A von Kármán vortex street can be seen traced in the low-level clouds south of Jan Mayen. (b) Sketch of the flight track for 294 showing stacks of three boundary layer legs (green), a sawtooth leg (red), and transit legs (blue). The letters indicate way points between Constable Point (CP) and Akureyri (A). The inset sketch shows the altitude of the legs flown at each stack.

We illustrate a typical mission (flight 294) in Fig. 7, showing a map of aircraft altitude overlaid on a visible satellite image. During this flight we sampled the structure of the ABL via a sawtooth cross section of four profiles and two stacks of straight and level legs at three heights that were immediately upstream and downstream of the *Alliance*. Figure 8 shows a cross section of potential temperature (θ), relative humidity w.r.t. ice (RH_i), and turbulent sensible heat flux based on the eddy covariance technique (e.g., Petersen and Renfrew 2009). It shows a more detailed snapshot of the cross section illustrated in Fig. 5. There is a cold surface layer (<100 m deep) overlying the MIZ, embedded within a near-neutral ABL of about 800 m depth. The RH_i shows an increase in moisture content to the east, consistent with the development of a shallow cumulus cloud deck, as apparent from satellite images at the time of the flight (e.g., Fig. 7). Turbulent sensible heat flux observations are surprisingly close to zero throughout most of the ABL and over the MIZ,

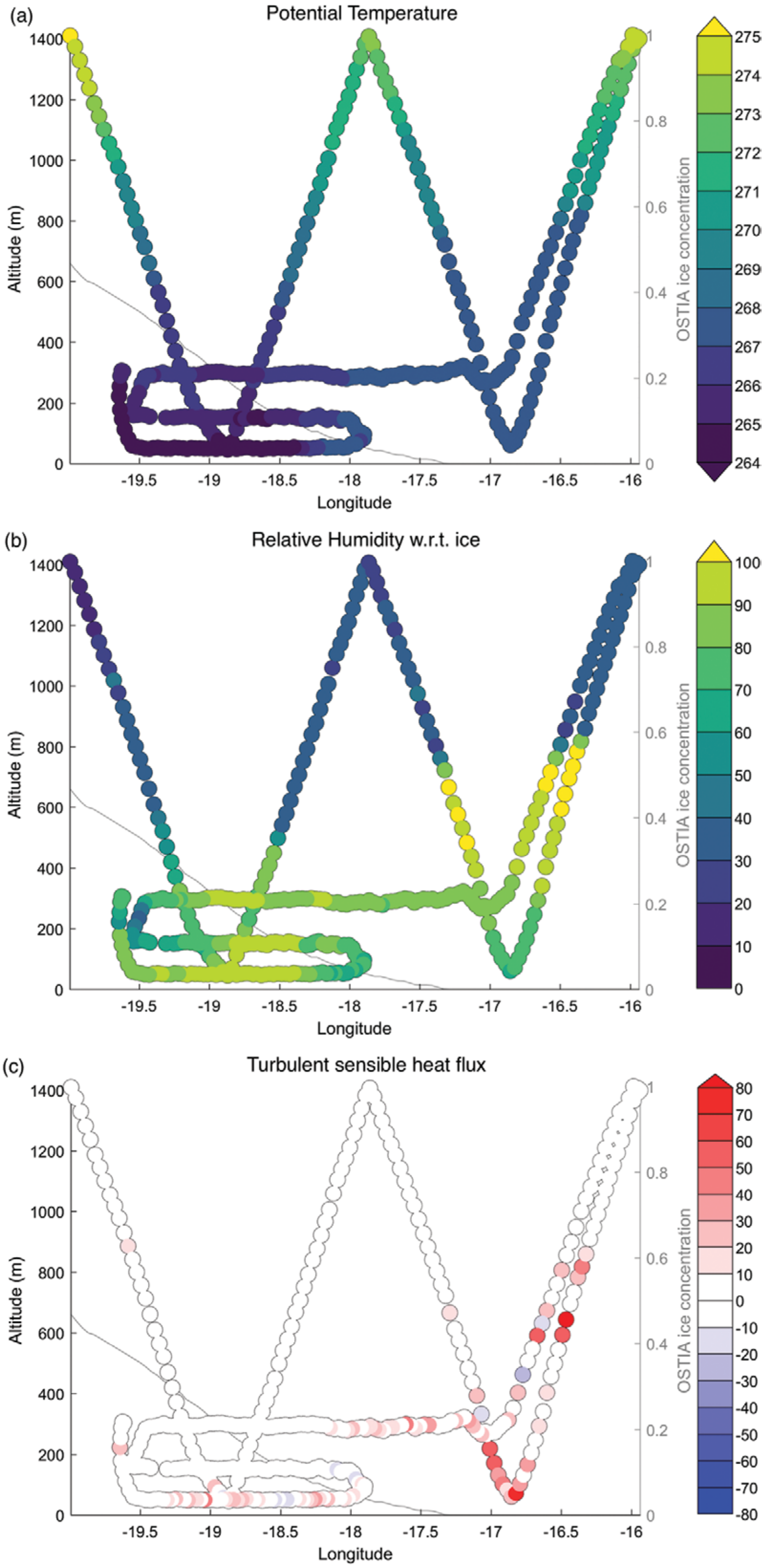

Fig. 8. Cross sections of (a) potential temperature (K), (b) relative humidity w.r.t. ice (%), and (c) turbulent sensible heat flux (W m^{-2}) from 1 Mar 2018 (flight 294). The cross section shows observations from sawtooth B to C and the three straight and level legs between D and E sketched in Fig. 7. Also shown is sea ice fraction, based on OSTIA data (gray lines; right-hand axis of each figure panel).

only reaching 10–20 W m^{-2} in places in the surface-layer leg over the MIZ. They are higher, up to 80 W m^{-2}, in the surface layer and around cloud level off the ice edge where there is also a systematic increase in the wind stress and turbulent kinetic energy (not shown). These sorts of observations of the turbulent structure of CAOs will be of great value in the evaluation of models and bulk flux algorithms.

Overall the aircraft campaign was highly successful. We coordinated research flights in the vicinity of the ship on three separate days (shaded in Table 2) during the development and evolution of the long-lived CAO over the Iceland Sea. This enabled the first simultaneous and coordinated water vapor isotope measurements from aircraft and ship. We have over 500 min of observations from the atmospheric surface layer—over 400 min during CAO conditions and over 200 min over sea ice—providing nearly 200 estimates of turbulent surface exchange. In addition, the ABL was thoroughly sampled with over 300 min of straight and level flying and 10 long (and 13 short) ABL sawtooth cross sections.

CLIMATE CONDITIONS DURING WINTER 2017/18.

To properly interpret our observations, it is important that we place our winter field campaign period into climatological context. Our region of interest is characterized by wintertime sea ice that has been retreating since the turn of the twentieth century, if not longer (Parkinson and Cavalieri 2008; Moore et al. 2015). Figure 9 shows the mean sea ice concentration in the region during January–March 2018, as well as the climatological mean concentration for 1979–2018 (data from Peng et al. 2013). The loss of sea ice in the region reflects a reduction in the width of the MIZ, from ~230 km during the 1980s to ~110 km during the 2010s. Also notable is the loss of a tongue of

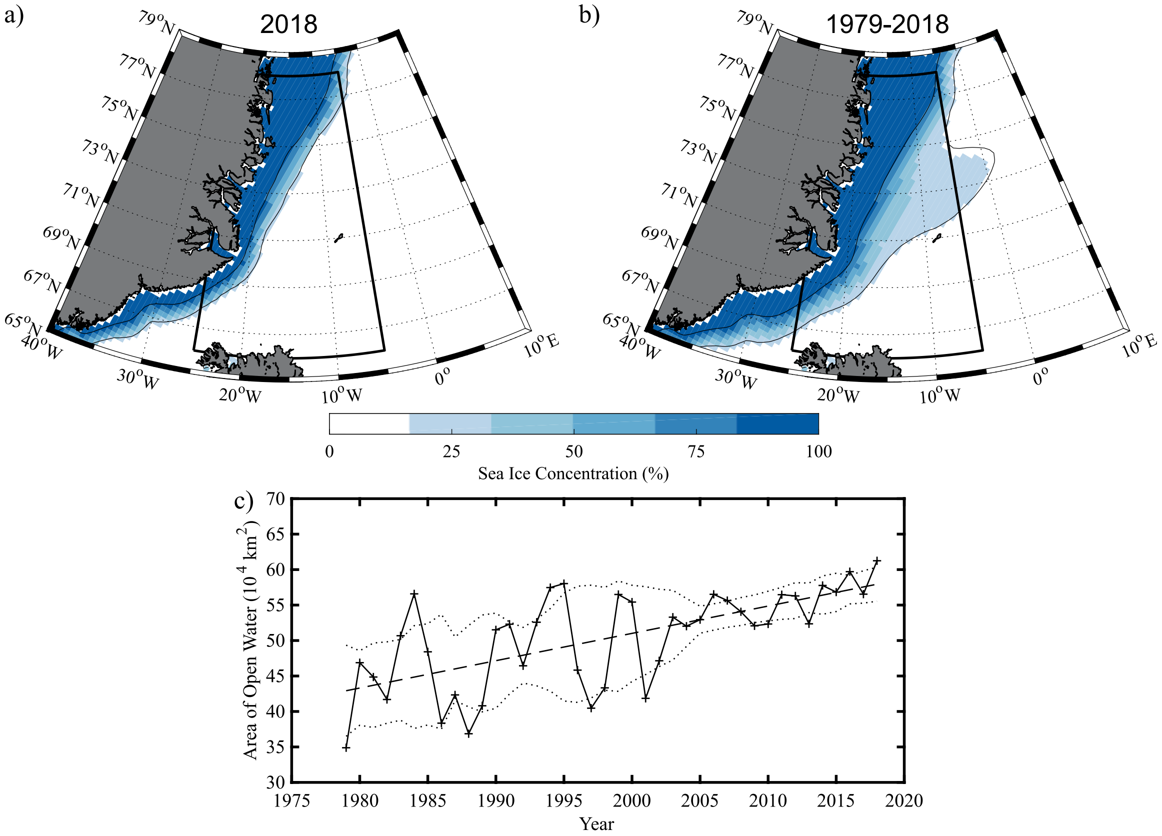

Fig. 9. Sea ice concentration for Jan–Mar: (a) for 2018 and (b) the mean for 1979–2018; contours at 15% and 80% are overlaid. (c) A time series of open water area for Jan–Mar 1979–2018, for the polygon shown in (a) and (b), plus the linear trend (38,000 km^2 decade^{-1}) and the 5-yr moving standard deviation about the linear trend. All data are from the NSIDC Climate Data Record.

sea ice known as the Odden ice tongue (Germe et al. 2011) that used to extend eastward over the Greenland Sea. Included in Fig. 9 is a time series of winter-mean open water area for the region. There is a 40-yr trend of increasing open water area (38,000 km^2 decade^{-1}) as well as pronounced interannual variability that reduced dramatically around 2000, associated with the loss of the Odden ice tongue (Rogers and Hung 2008). As discussed by Moore et al. (2015) and Våge et al. (2018), this sea ice retreat has profound implications for the intensity of ocean convection in the Iceland and Greenland Seas.

Atmospheric conditions during the field phase of the experiment were influenced by the occurrence of a sudden stratospheric warming (SSW) as well as a transition from NAO positive to NAO negative conditions. An SSW index (Charlton and Polvani 2007) indicates the SSW occurred on 8 February 2018 (the transition to negative values), while an NAO index (Barnston and Livezey 1987) indicates a transition on 26 February 2018 (Fig. 10). These two events are related (Moore et al. 2018), in that NAO negative conditions typically occur as part of a delayed tropospheric response to a SSW (Baldwin and Dunkerton 2001; Kolstad et al. 2010). A sea level pressure (SLP) time series—from European Centre for Medium-Range Weather Forecasts (ECMWF) interim reanalysis (ERA-I) data (Dee et al. 2011) averaged over the oceanic area of interest shown in Fig. 9—illustrates these two drivers (Fig. 10c). In particular, there was anomalously high SLP [in excess of two standard deviations (σ) above the mean] throughout the region in late February and early March. This was likely the transient response to the SSW that led to high pressures and cold temperatures over northern Europe (Moore et al. 2018). It was also coincident with a sharp transition to NAO negative conditions.

The 10-m wind speeds over the study region were on average close to the climatological mean, although there was significant variability (Fig. 10d). In contrast, the ERA-I near-surface air temperatures were anomalously warm throughout the period of interest, with mean values 1σ above the climatological mean (exceeding 2σ above the mean during the SSW, Fig. 10e). This period of extreme warmth was associated with a strong meridional pressure gradient that resulted in above-freezing conditions in north Greenland (Moore et al. 2018). The end of the SSW and the transition to NAO negative conditions resulted in a dramatic drop in air temperatures around 1 March 2018; this was the start of the long-lived CAO over the Iceland Sea sampled in detail during the IGP (see Table 2 and Figs. 4, 5, 7, 8). Forecast charts showing the early stages of this CAO and its likelihood of occurrence are discussed below. The CAO lasted more than 10 days, but did not bring a particularly cold air mass over the region—temperatures stayed typically around –5°C, just above the long-term mean. Associated with the CAO were elevated surface turbulent heat fluxes, peaking at 200 W m^{-2} (Fig. 10f). This is in contrast with the below-average heat fluxes of the first half of the IGP period, which were especially low during the SSW. We note that a second, stronger CAO occurred over the Greenland Sea toward the end of the IGP period, starting on 16 March (Table 2). This event, however, is not very clear in Fig. 10 because of the large averaging area.

LONGER-TERM OBSERVATIONS. *Gliders.* We had planned on carrying out a comprehensive survey of the Iceland and Greenland Seas using autonomous ocean gliders for the duration of winter 2017/18. The gliders were upgraded with ice avoidance software to operate more safely in the MIZ (e.g., Curry et al. 2014). However, a series of sensor failures, pump failures, and communication problems limited the glider measurement program to a few weeks in early January in the Greenland Sea, and to mid-February to mid-April in the Iceland Sea. The latter glider operated primarily between the ice edge and the location of the subsurface mooring and meteorological buoy in the Eggvin Offset (Fig. 2), a deep passage between the West Jan Mayen Ridge and the Kolbeinsey Ridge

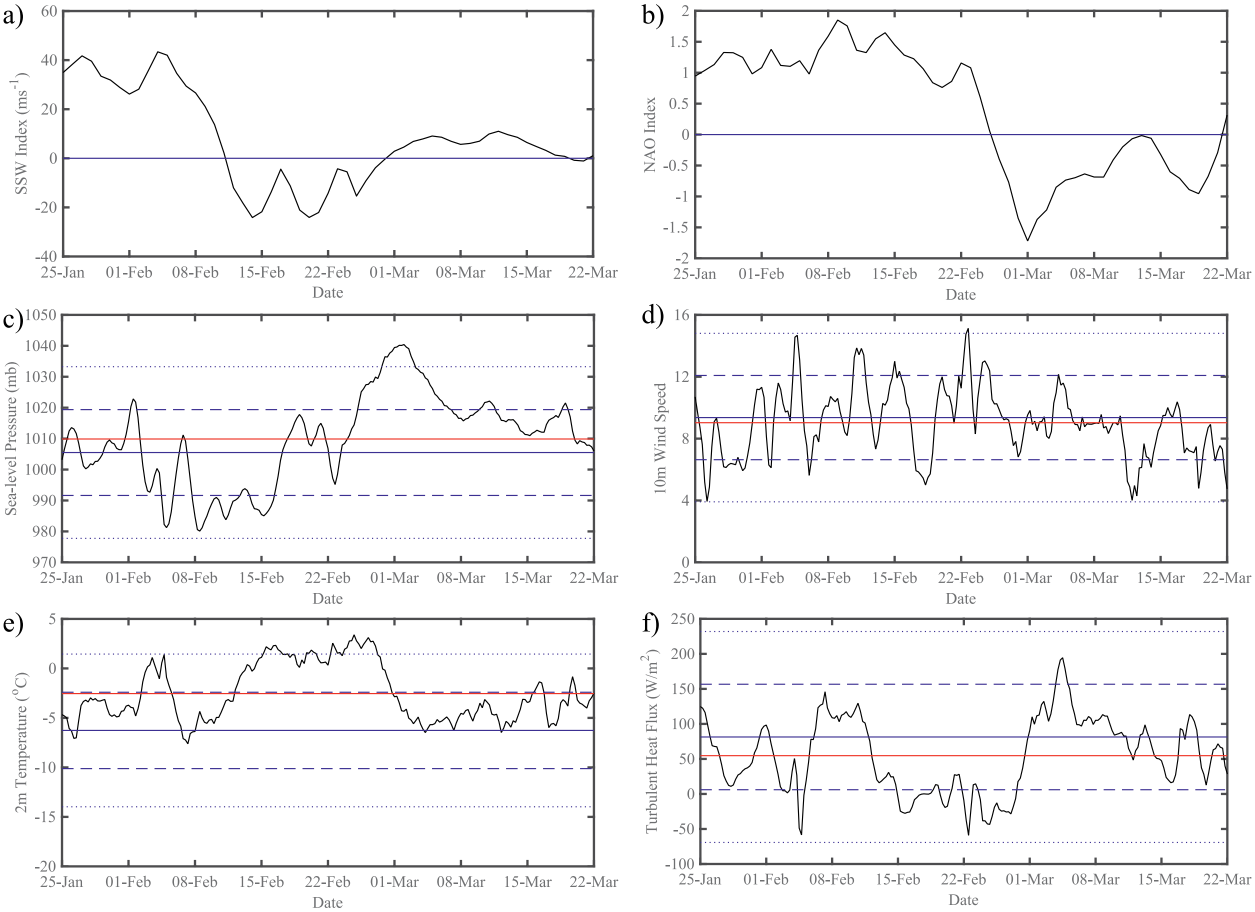

Fig. 10. Time series from the IGP field campaign period in Jan–Mar 2018. (a) An SSW index (m s^{-1}), (b) an NAO index, (c) SLP (mb), (d) 10-m wind speed (m s^{-1}), (e) 2-m air temperature, and (f) the total surface turbulent heat flux (W m^{-2}). The time series in (c)–(f) are all averaged over the oceanic region bounded by 66°N, 40°W and 78°N, 5°E. Also shown in (c)–(f) are the campaign-period mean (red line) and the climatological mean, as well as the 1 and 2σ above/below that mean (blue solid, dashed, and dotted lines) for the period 1979–2018.

(see the mooring discussion below). The transect was the same as that previously occupied by a glider in winter 2015/16 (Våge et al. 2018).

A comparison between the February 2016 transect, which did not extend very close to the ice edge, and the IGP glider transects from March and April 2018, which nearly reached the East Greenland Current, demonstrate that the ocean mixed layer during the 2017/18 winter was substantially shallower, warmer, and less dense than in winter 2015/16 (Fig. 11). Despite this, the Atlantic-origin water (density > 27.8 kg m^{-3} and T > 0°C) that was being transported toward Denmark Strait by the East Greenland Current was ventilated by the end of the weaker 2017/18 (IGP) winter, as evident in the bottom panel of Fig. 11. This implies that transformation of this water mass in the Iceland Sea is not dependent on severe winter conditions and may occur regularly when the East Greenland Current is ice-free (Våge et al. 2018).

Unfortunately, our attempts during the *Alliance* cruise to directly quantify the turbulent mixing rates associated with water-mass transformation via glider-based microstructure measurements were unsuccessful due to glider malfunctions. As such, we will attempt to infer transformation rates using indirect mixing rate estimates from the glider data collected; specifically by using our finescale vertical velocity and density measurements to infer dissipation via the large-eddy method (Beaird et al. 2012), and using our finescale density measurements to infer dissipation from a strain-based parameterization (e.g., Johnston and Rudnick 2015).

Moorings. We deployed subsurface ocean moorings at two locations during the IGP from summer 2016 to summer 2018. These deployments relied on a number

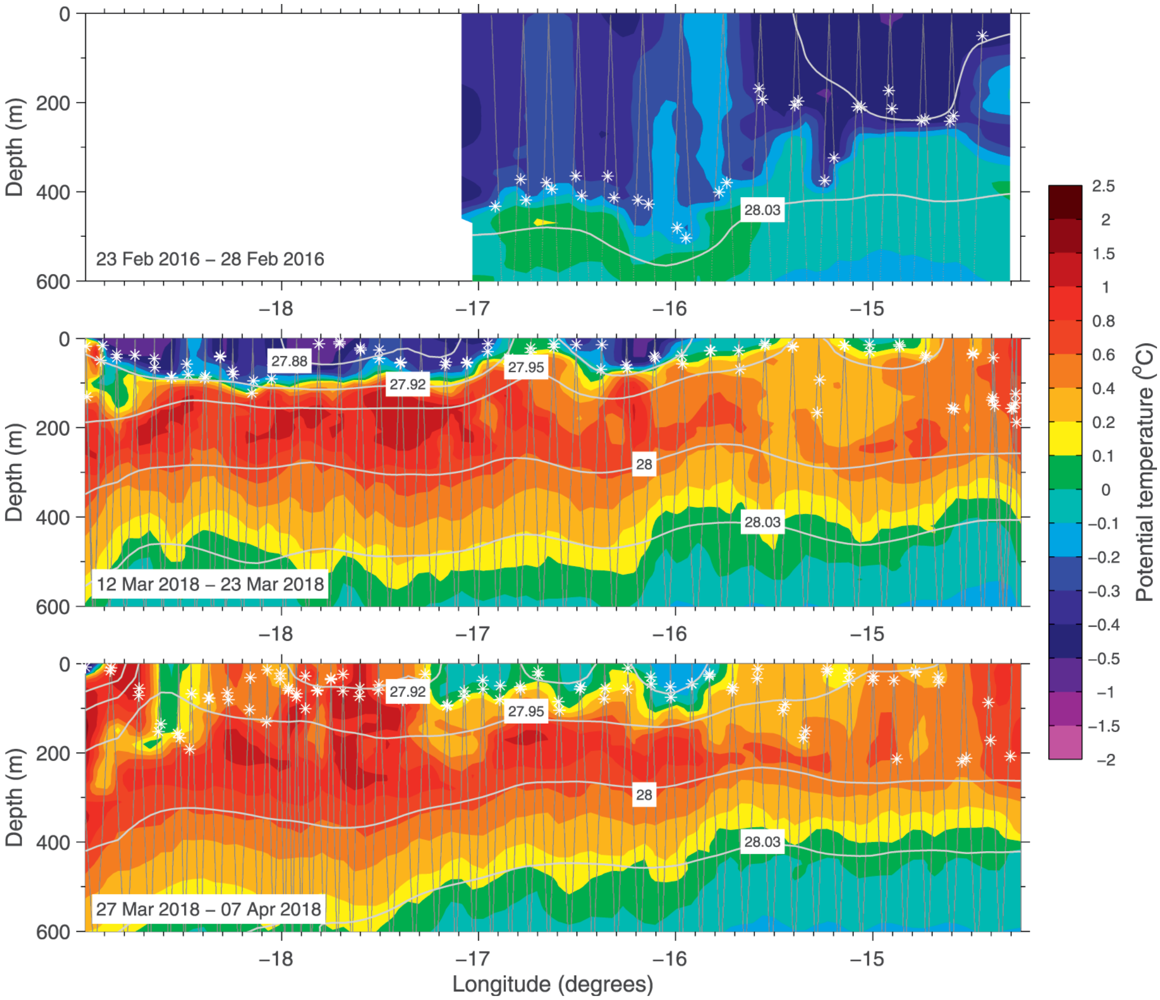

Fig. 11. Ocean cross sections of potential temperature across the east Greenland continental slope to Eggvin Offset near 71°N, derived from glider observations: (top) Feb 2016 (from Våge et al. 2018), (middle) Mar 2018, and (bottom) Mar–Apr 2018. Selected isopycnals (gray contours) and mixed layer depths (stars) are overlaid.

of additional research cruises or additional time on monitoring cruises. First, an array of four moorings was deployed across the NIJ north of Iceland (see Fig. 2a for location). The moorings were placed on the Slétta repeat hydrographic transect near 16°W that is occupied four times a year by the Icelandic Marine and Freshwater Research Institute. This represents the first mooring array deployed across the current to the east of the Kolbeinsey Ridge, where previously there have been only snapshots from shipboard hydrographic/velocity surveys (Våge et al. 2011; Semper et al. 2019). These continuous, long-term measurements will shed light on the magnitude and properties of the NIJ only a short distance downstream of where it is thought to originate. They will also provide a contrast to the previous moored measurements of the NIJ from the Kögur line to the west of the Kolbeinsey Ridge (Harden et al. 2016).

Second, a single subsurface mooring was deployed in the Eggvin Offset on the northern end of the Kolbeinsey Ridge (near 70°N, 16°W; see Fig. 2b)—in the northwest part of the Iceland Sea, where the deepest mixed layers were expected to be found (Våge et al. 2015). We chose this location to be in ice-free waters through winter, but sufficiently close to the ice edge so that it would be subject to high ocean–atmosphere heat fluxes during intense CAOs. The mooring was equipped with a combination of point hydrographic instruments and temperature loggers sampling at high frequency (see Table 1). The vertical resolution was 25 m in the upper 300 m of the water column, then every 50 m down to 800 m in order to monitor the wintertime evolution of the mixed layer. Profiling current meters covered most of the water column above 700 m. Preliminary analysis indicates that the ocean mixed layer was deeper, colder, and denser in winter 2016/17 relative to the 2017/18 winter (Fig. 12). But even during the weaker IGP winter there were mixed layers up to 200 m deep and colder than 0.3°C by the end of the convective season.

Meteorological buoy. During the first part of the *Alliance* cruise a Seawatch Wavescan meteorological buoy was deployed adjacent to the subsurface mooring in the Eggvin Offset in the northwest Iceland Sea. The buoy was configured to record standard meteorological variables, sea surface temperature (SST) and surface ocean currents every hour (see Table 1). The buoy worked well for 2.5 months, until it broke loose from its anchor and stopped recording on 6 May 2018. It was recovered soon after.

FORECASTING AND COORDINATING ACTIVITIES.

To inform day-to-day operations and plan research flights, we made use of several bespoke weather forecasts during the campaign period. The Met Office ran a limited-area 48-h forecast using their operational Met Office Unified Model (MetUM) for the Iceland Sea region in support of the IGP, while the Icelandic Met Office (IMO) and their partners at the Danish Meteorological Institute (DMI) gave us access to a trial HARMONIE-AROME (HIRLAM–ALADIN Research on Mesoscale Operational NWP in Euromed–Applications of Research to Operations at Mesoscale) 48–66-h forecast that encompassed the same region. Both models were convection-permitting, with horizontal grid sizes of 2.2 and 2.5 km, respectively. The Met Office forecasts were initialized twice daily from their global operational system, while the DMI–IMO forecasts were run with 3-hourly three-dimensional variational data assimilation

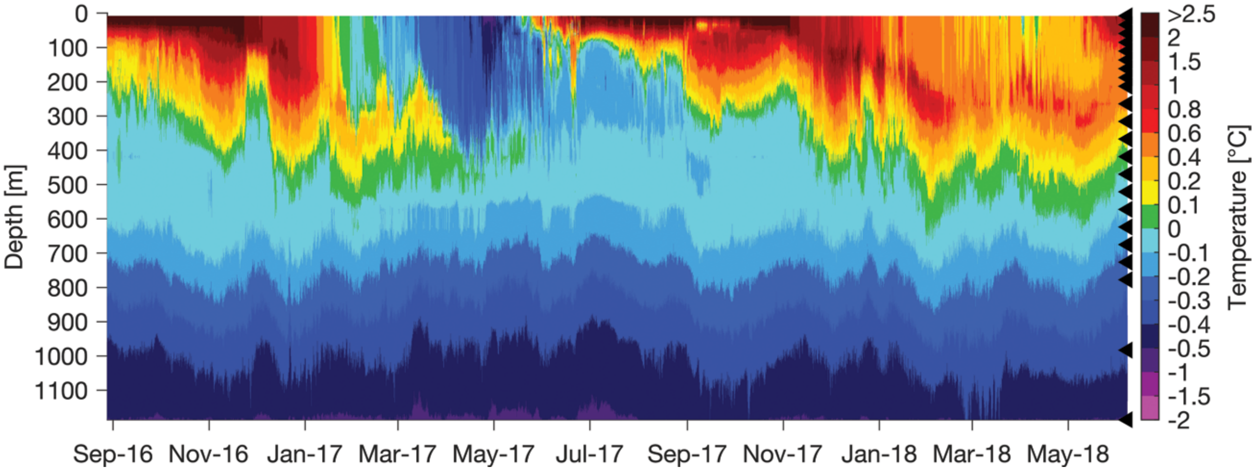

Fig. 12. Ocean temperature time series from a mooring at the Eggvin Offset (70.6°N, 15.6°W). The temperature cross section consists of observations from 22 depths (black triangles) every 2 h.

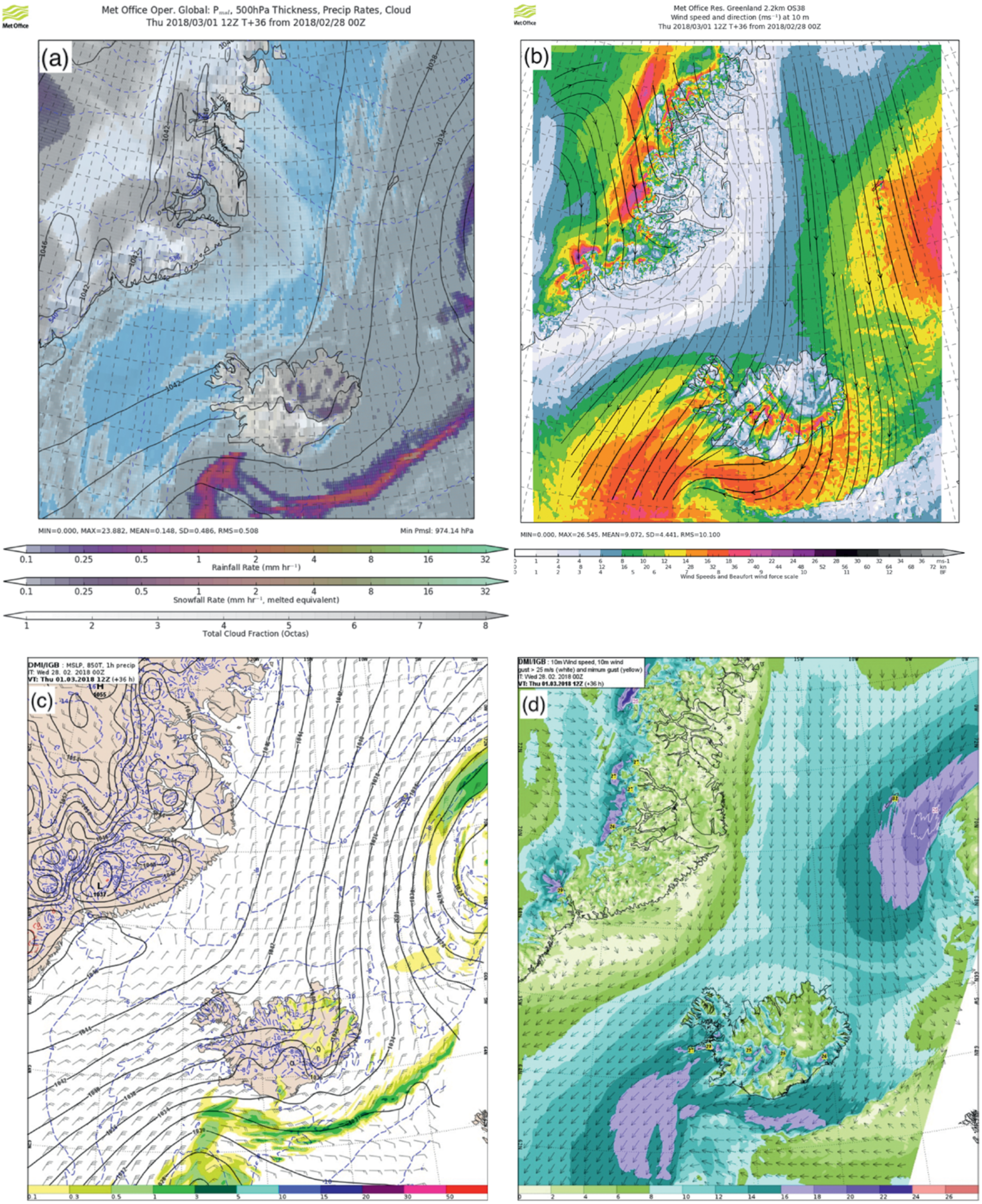

Fig. 13. Forecast charts for 1200 UTC 1 Mar 2018 (*T* + 36 h) showing (a) SLP (black lines), 500-hPa thickness (blue dashed lines), cloud cover (gray shading), and precipitation (shading); (b) 10-m wind speed and streamlines; (c) SLP (black lines), 850-hPa temperature (blue dashed lines), 10-m wind vectors (barbs), and precipitation (shading); (d) 10-m wind speed and wind vectors. The top panels are from the Met Office, the bottom panels are plotted by the IMO, from forecasts by the DMI.

(a) CAO probability

1200 UTC 20180301 (+108 h)

(d) CAO probability

1200 UTC 20180302 (+132 h)

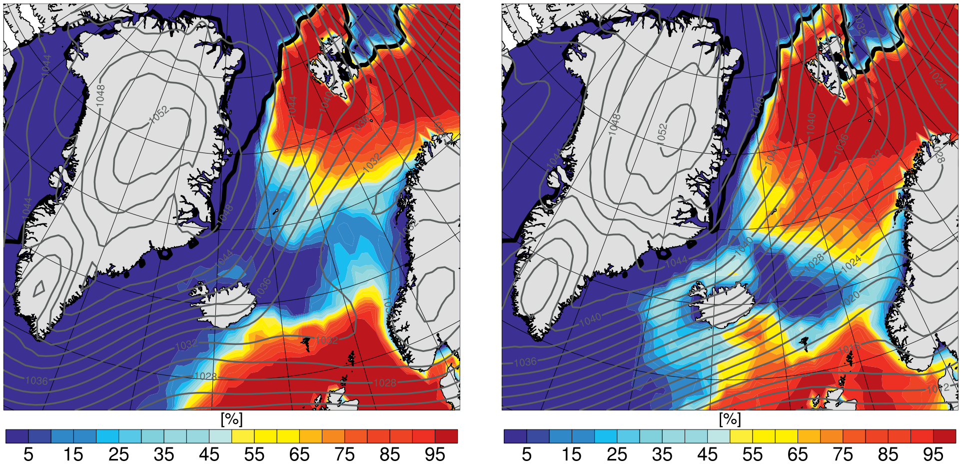

(b) ens. mean CAO index

1200 UTC 20180301 (+108 h)

(e) ens. mean CAO index

1200 UTC 20180302 (+132 h)

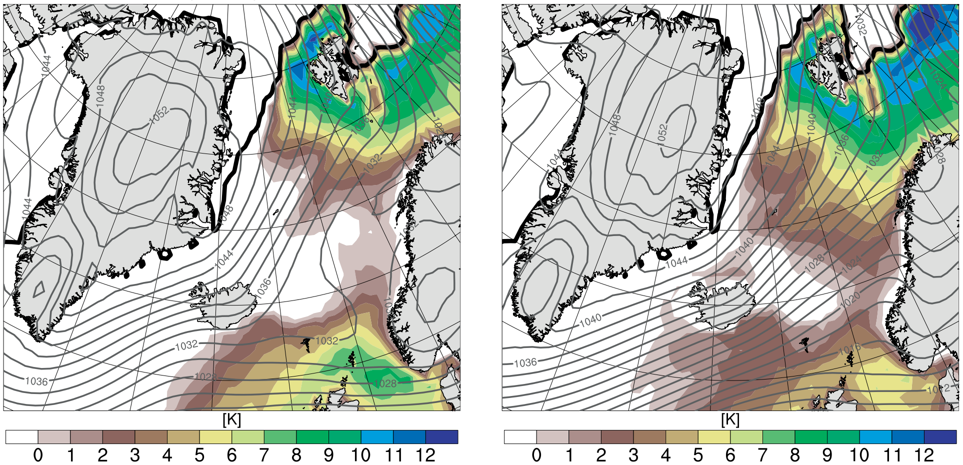

(c) ens. mean sensible heat flux

1200 UTC 20180301 (+108 h)

(f) ens. mean sensible heat flux

1200 UTC 20180302 (+132 h)

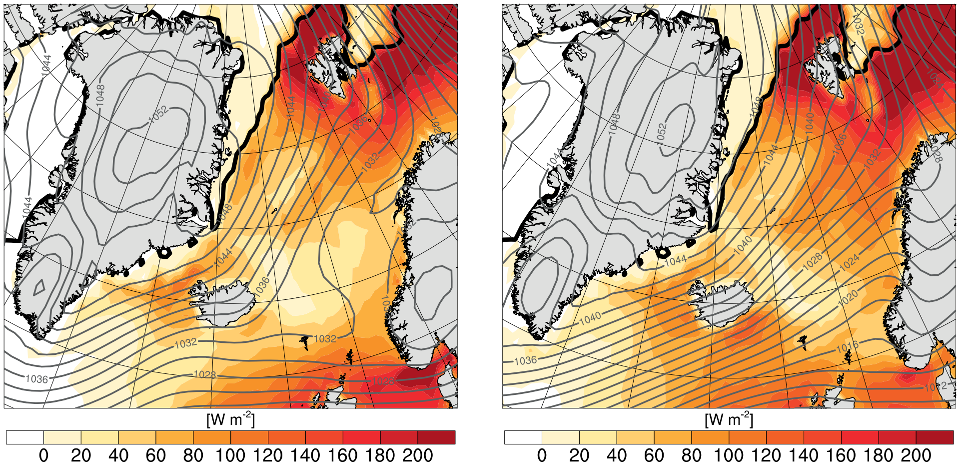

Fig. 14. Cold-air outbreak diagnostics based on 50 ECMWF ensemble prediction system members: (a),(d) the probability of a cold-air outbreak of strength $\Delta\theta > 2$ K (where $\Delta\theta = \theta_{\mathrm{SST}} - \theta_{850\mathrm{hPa}}$); (b),(e) the ensemble-mean CAO magnitude (i.e., $\Delta\theta$); and (c),(f) the ensemble-mean surface sensible heat flux. All panels have the ensemble-mean SLP field contoured (gray lines every 2 hPa) and the 50% sea ice concentration contour (thick black line). Forecasts are for (left) 4.5 days (T + 108 h) and (right) 5.5 days (T + 132 h) from 0000 UTC 25 Feb 2018, which are valid at 1200 UTC 1 Mar and 2 Mar 2018 as indicated.

(3DVAR). We had access to a comprehensive set of charts from both these forecasts and the respective global operational forecasts. The Met Office forecasts included specialized diagnostics which were important for flight planning, such as maps of cloud base height and surface sensible heat flux as well as cross sections of potential temperature and cloud liquid water. We also converted all the charts into georeferenced files (tiff and kmz formats) to allow import into flight-planning tools. Figure 13 shows 36-h forecast charts for 1200 UTC 1 March 2018, the same day highlighted in Figs. 4, 5, 7, and 8. Indeed, a comparison against Fig. 7 illustrates the overall high quality of the forecast cloud field. The two forecasts are very similar, showing the meridional orientation of the isobars and northerly winds associated with the early stages of the CAO. In the Iceland Sea, the 10-m winds increase from around 4 to 12 m s^{-1} in the MetUM forecast and from around 6 to 14 m s^{-1} in the HARMONIE–AROME forecast—broadly consistent with the observed winds (Figs. 4, 5). To the south of Iceland there is a coherent band of precipitation at the leading edge of the CAO that is similar in location and magnitude in both forecasts. Notably, there are convective snow showers behind this rainband, to the southeast of Iceland, that are not forecast in the global models (not shown).

To inform medium-term field operations and coordination between the *Alliance* team and the aircraft team, we developed a probability-based forecast for our primary meteorological science target: cold-air outbreaks. We used the 50 members of the ECMWF ensemble prediction system to estimate the likelihood of a CAO up to 10 days ahead, based on a well-established CAO index ($\Delta\theta = \theta_{SST} - \theta_{850hPa}$); see Papritz and Spengler (2017). A positive CAO index indicates an atmosphere that is colder than the ocean and so is characterized by upward surface sensible heat fluxes. Figure 14 shows the probability of a CAO 4.5 and 5.5 days ahead, as well as the ensemble-mean CAO strength and the associated surface sensible heat flux (we could also examine individual ensemble members). Figure 14 indicates a >90% probability of a CAO over the northern Greenland Sea and ~30% probability of a CAO over the eastern Iceland Sea on 1 March 2018, with the likelihood of a CAO clearly increasing and extending over the entire Iceland Sea for the next day. This sort of lead time enabled us to coordinate our observing program, for example, guiding both the ship and aircraft planning to capture the onset and development of this CAO (see Table 2). As the forecast lead time reduced, the probability of this CAO occurring over the Iceland Sea steadily increased, giving us further confidence in our planned operations. The forecast was for relatively mild conditions, with typical surface sensible heat fluxes of around 100 W m^{-2} (Fig. 14), broadly consistent with the short-range forecasts available closer to the event.

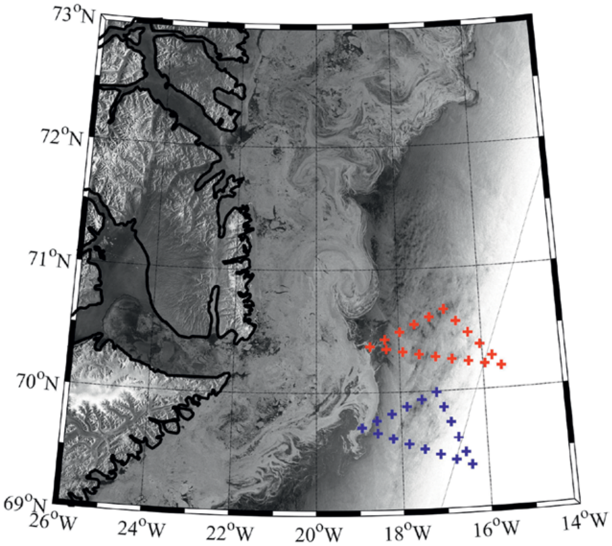

Fig. 15. Sentinel SAR image of the MIZ off east Greenland at 0800 UTC 3 Mar 2018 showing the complex small-scale variability associated with ocean eddies and fronts that impact the sea ice distribution. Lighter shading is from a higher reflectivity surface. Annotated in blue and red are the two survey triangles that the *Alliance* carried out during 1–6 Mar 2018.

Coordination between the *Alliance* and the aircraft teams—and ship operations in general—were greatly aided by access to a subset of these forecast charts on the winter cruise. Due to the limited bandwidth at these latitudes, we transferred a selection of key charts, including mean sea level pressure, near-surface winds, and ocean wave heights. We supplemented the charts with a short daily text forecast specifically for the *Alliance*’s location, as well as a separate text forecast from DMI. Sea ice imagery was also vital for operational planning. Three products were emailed daily to the ship: an ice image from the Sentinel satellite from DMI; a digital ice concentration file from Advanced Microwave Scanning Radiometer 2 (AMSR2); and a high-resolution Sentinel synthetic aperture radar (SAR) generated by the University of Toronto (e.g., Fig. 15). The latter product included the planned sampling locations of the ship for the next 24 h. These three ice products allowed us to visualize conditions in the MIZ, providing valuable context for maneuvering the ship. As a general rule we would aim to begin each approach into the MIZ at first light, maximizing the number of daylight hours for station work in and near the ice. Of particular concern was the impact on ship operations of small-scale ice features within the MIZ, including eddies and filaments (e.g., Manucharyan and Thompson 2017); a striking example is shown in Fig. 15.

We incorporated the forecast charts and sea ice products into *Alliance*'s daily operational briefings on the ship, which was invaluable for planning our science activities. We also exchanged our planned operations between the *Alliance* and the aircraft team on a daily basis. When possible, we shared detailed information for the next day and broader guidance for the following few days. This allowed more time to prepare flight missions and schedule ship activities; it also acted as insurance for when the ship lost communication (a regular occurrence when north of 70°N). The daily update from the *Alliance* always included a map of the locations of recent CTD casts as well as predictions of forthcoming ones, while the daily update from the aircraft team included plans for flying over the next few days. This information exchange was time consuming but essential for achieving the high levels of coordination we desired, for example, coordinating a repeat ship survey or an intensive period of radiosonde launches (cf. Table 2).

FUTURE PLANS. The Iceland Greenland Seas Project has obtained an unprecedented set of coordinated, detailed observations of the ocean and atmosphere during winter in the subpolar seas. Analysis of this wealth of data is well underway. Our coordinated approach will continue throughout the analysis and numerical modeling activities (see sidebar). It is also embedded within broader YOPP activities, for example, making use of additional forecast products and diagnostics. Over the next few years we anticipate a number of studies addressing our project hypothesis and objectives, by examining, among other things, the anatomy of a cold-air outbreak, air–sea fluxes over the MIZ, ABL development over the MIZ, the relationship between CAOs and polar lows, the origin and characteristics of

NUMERICAL MODELING PLANS

Numerical modeling of the atmosphere, ocean, and climate system is being carried out in parallel to the observational component of the IGP. Here we describe a few activities as illustrations.

A set of regional climate modeling experiments have been run to investigate the impact of anomalous distributions of sea ice on the frequency and magnitude of high heat flux events in the Iceland and Greenland Seas. We have used the MetUM in atmosphere-only mode with a regional domain (62°–79°N, 40°E–5°W) run at 8-km grid size and nested within a global model. The global model was initialized daily from ERA-I reanalyses and was used to force the regional model at the lateral boundaries. We have run simulations for 20 years with four different sets of daily-updated sea ice and SST surface conditions:

i) a baseline simulation with time varying sea ice and SSTs concomitant with the date of the simulation;
ii) a maximum ice simulation with annually-repeating sea ice and SSTs from 1987/88—the winter with the greatest sea ice extent in the Iceland–Greenland Seas region;
iii) a median ice simulation with annually repeating sea ice and SSTs from 2003/04—the winter with sea ice extent closest to the median value in the region; and
iv) a minimum ice simulation with annually repeating sea ice and SSTs from 2015/16—the winter with the smallest sea ice extent in the region.

Through this experimental design we are now examining how changes in sea ice concentration and extent influence the distribution, frequency, and magnitude of high heat flux events. Interestingly, the role of the extreme sea ice distributions acts differently in the two seas, a result we are now exploring in more detail.

We are running two classes of ocean models in support of the IGP. The first is a realistic, regional primitive equation model with a coupled dynamic/thermodynamic sea ice model that extends from south of Denmark Strait to 79°N, and from Greenland to Norway. This model is forced with fluxes of heat, freshwater, and momentum derived from atmospheric reanalysis using bulk formulae and has open northern and southern boundaries, as in Almansi et al. (2017). We will run it for different time periods, to cover the different regimes of the NAO, and also for the winter of 2017/18 to compare with the in situ IGP observations. We seek to understand where, when, and how the densest waters are formed under different atmospheric conditions, and how they are subsequently advected from these source regions across the sills to the south.

Our second class of ocean models is focused on the influence of wind and surface heat loss on convection in the transition region between the relatively buoyant East Greenland Current and the denser waters offshore. Observations indicate that the low-salinity water from the shelf is transported offshore in small, thin patches and eddies, where it can then inhibit deep convection and water-mass transformation. The model will be used to understand what controls the offshore flux of freshwater, the amount of water-mass transformation, and the depth of deep convection.

precipitation over the Nordic Seas, ABL turbulent fluxes downstream of orography, the heat budget of a coupled ocean–atmosphere column, water-mass modification in the northwest Iceland Sea and southwest Greenland Sea, the impact of small-scale ocean variability and atmospheric wind and buoyancy forcing on convective overturning, the circulation of dense water, and the ventilation/formation of the NIJ. We anticipate such a body of work will lead to a transformation in our understanding of how the coupled ocean–atmosphere–ice system in the Nordic Seas impacts the lower limb of the AMOC.

ACKNOWLEDGMENTS. The IGP has received funding from the U.S. National Science Foundation: Grant OCE-1558742; the U.K.'s Natural Environment Research Council: AFIS (NE/N009754/1); the Research Council of Norway: MOCN (231647), VENTILATE (229791), SNOWPACE (262710) and FARLAB (245907); and the Bergen Research Foundation (BFS2016REK01). We thank all those involved in the field work associated with the IGP, particularly the officers and crew of the *Alliance*, and the operations staff of the aircraft campaign.

REFERENCES

Achtert, P., I. M. Brooks, B. J. Brooks, B. I. Moat, J. Prytherch, P. O. G. Persson, and M. Tjernström, 2015: Measurement of wind profiles over the Arctic Ocean from ship-borne Doppler lidar. *Atmos. Meas. Tech.*, **8**, 4993–5007, https://doi.org/10.5194/amt-8-4993-2015.

Almansi, M., T. W. N. Haine, R. S. Pickart, M. G. Magaldi, R. Gelderloos, and D. Mastropole, 2017: High-frequency variability in the circulation and hydrography of the Denmark Strait overflow from a high-resolution numerical model. *J. Phys. Oceanogr.*, **47**, 2999–3013, https://doi.org/10.1175/JPO-D-17-0129.1.

Baldwin, M. P., and T. J. Dunkerton, 2001: Stratospheric harbingers of anomalous weather regimes. *Science*, **294**, 581–584, https://doi.org/10.1126/science.1063315.

Barnston, A. G., and R. E. Livezey, 1987: Classification, seasonality and persistence of low-frequency atmospheric circulation patterns. *Mon. Wea. Rev.*, **115**, 1083–1126, https://doi.org/10.1175/1520-0493(1987)115<1083:CSAPOL>2.0.CO;2.

Beaird, N., I. Fer, P. Rhines, and C. Eriksen, 2012: Dissipation of turbulent kinetic energy inferred from Seagliders: An application to the eastern Nordic Seas overflows. *J. Phys. Oceanogr.*, **42**, 2268–2282, https://doi.org/10.1175/JPO-D-12-094.1.

Böning, C. W., E. Behrens, A. Biastoch, K. Getzlaff, and J. L. Bamber, 2016: Emerging impact of Greenland meltwater on deepwater formation in the North Atlantic Ocean. *Nat. Geosci.*, **9**, 523–527, https://doi.org/10.1038/ngeo2740.

Bourassa, M.A., and Coauthors, 2013: High-latitude ocean and sea ice surface fluxes: Challenges for climate research. *Bull. Amer. Meteor. Soc.*, **94**, 403–423, https://doi.org/10.1175/BAMS-D-11-00244.1.

Boutle, I. A., J. E. J. Eyre, and A. P. Lock, 2014: Seamless stratocumulus simulation across the turbulent gray zone. *Mon. Wea. Rev.*, **142**, 1655–1668, https://doi.org/10.1175/MWR-D-13-00229.1.

Brümmer, B., 1997: Boundary layer mass, water, and heat budgets in wintertime cold-air outbreaks from the Arctic sea ice. *Mon. Wea. Rev.*, **125**, 1824–1837, https://doi.org/10.1175/1520-0493(1997)125<1824:BLMWAH>2.0.CO;2.

Buckley, M. W., and J. Marshall, 2016: Observations, inferences, and mechanisms of the Atlantic Meridional Overturning Circulation: A review. *Rev. Geophys.*, **54**, 5–63, https://doi.org/10.1002/2015RG000493.

Caesar, L., S. Rahmstorf, A. Robinson, G. Feulner, and V. Saba, 2018: Observed fingerprint of a weakening Atlantic Ocean overturning circulation. *Nature*, **556**, 191–196, https://doi.org/10.1038/s41586-018-0006-5.

Cassou, C., L. Terray, J. W. Hurrell, and C. Deser, 2004: North Atlantic winter climate regimes: Spatial asymmetry, stationarity with time, and oceanic forcing. *J. Climate*, **17**, 1055–1068, https://doi.org/10.1175/1520-0442(2004)017<1055:NAWCRS>2.0.CO;2.

Charlton, A. J., and L. M. Polvani, 2007: A new look at stratospheric sudden warmings. Part I: Climatology and modeling benchmarks. *J. Climate*, **20**, 449–469, https://doi.org/10.1175/JCLI3996.1.

Condron, A., and I. A. Renfrew, 2013: The impact of polar mesoscale storms on northeast Atlantic Ocean circulation. *Nat. Geosci.*, **6**, 34–37, https://doi.org/10.1038/ngeo1661.

Curry, B., C. M. Lee, B. Petrie, R. E. Moritz, and R. Kwok, 2014: Multiyear volume, liquid freshwater, and sea ice transports through Davis Strait, 2004–10. *J. Phys. Oceanogr.*, **44**, 1244–1266, https://doi.org/10.1175/JPO-D-13-0177.1.

Dee, D. P., and Coauthors, 2011: The ERA-Interim reanalysis: Configuration and performance of the data assimilation system. *Quart. J. Roy. Meteor. Soc.*, **137**, 553–597, https://doi.org/10.1002/qj.828.

de Roode, S. R., and Coauthors, 2019: Turbulent transport in the gray zone: A large eddy model intercomparison study of the CONSTRAIN cold air outbreak case. *J. Adv. Model. Earth Syst.*, **11**, 597–623, https://doi.org/10.1029/2018MS001443.

Elvidge, A. D., I. A. Renfrew, A. I. Weiss, I. M. Brooks, T. A. Lachlan-Cope, and J. C. King, 2016: Observations of surface momentum exchange over the marginal-ice-zone and recommendations for its parameterization. *Atmos. Chem. Phys.*, **16**, 1545–1563, https://doi.org/10.5194/acp-16-1545-2016.

Fiedler, E., T. Lachlan-Cope, I. A. Renfrew, and J. C. King, 2010: Convective heat transfer of thin-ice covered polynyas. *J. Geophys. Res.*, **115**, C10051, https://doi.org/10.1029/2009JC005797.

Germe, A., M.-N. Houssais, C. Herbaut, and C. Cassou, 2011: Greenland Sea sea ice variability over 1979-2007 and its link to the surface atmosphere. *J. Geophys. Res.*, **116**, C10034, https://doi.org/10.1029/2011JC006960.

Glessmer, M. S., T. Eldevik, K. Våge, J. E. Ø. Nilsen, and E. Behrens, 2014: Atlantic origin of observed and modelled freshwater anomalies in the Nordic Seas. *Nat. Geosci.*, **7**, 801–805, https://doi.org/10.1038/ngeo2259.

Harden, B. E., I. A. Renfrew, and G. N. Petersen, 2011: A climatology of wintertime barrier winds off southeast Greenland. *J. Climate*, **24**, 4701–4717, https://doi.org/10.1175/2011JCLI4113.1.

——, ——, and ——, 2015: Meteorological buoy observations from the central Iceland Sea. *J. Geophys. Res. Atmos.*, **120**, 3199–3208, https://doi.org/10.1002/2014JD022584.

——, and Coauthors, 2016: Upstream sources of the Denmark Strait Overflow: Observations from a high-resolution mooring array. *Deep-Sea Res. I*, **112**, 94–112, https://doi.org/10.1016/j.dsr.2016.02.007.

Holte, J., and F. Straneo, 2017: Seasonal overturning of the Labrador Sea as observed by Argo floats. *J. Phys. Oceanogr.*, **47**, 2531–2543, https://doi.org/10.1175/JPO-D-17-0051.1.

Jahnke-Bornemann, A., and B. Brümmer, 2008: The Iceland-Lofoten pressure difference. *Tellus*, **61A**, 466–475, https://doi.org/10.1111/j.1600-0870.2009.00401.x.

Johnston, T. M. S., and D. L. Rudnick, 2015: Trapped diurnal internal tides, propagating semidiurnal internal tides, and mixing estimates in the California Current System from sustained glider observations, 2006–2012. *Deep-Sea Res. II*, **112**, 61–78, https://doi.org/10.1016/j.dsr2.2014.03.009.

Jónsson, S., and H. Valdimarsson, 2004: A new path for the Denmark Strait overflow water from the Iceland Sea to Denmark Strait. *Geophys. Res. Lett.*, **31**, L03305, https://doi.org/10.1029/2003GL019214.

Jung, T., S. Serrar, and Q. Wang, 2014: The oceanic response to mesoscale atmospheric forcing. *Geophys. Res. Lett.*, **41**, 1255–1260, https://doi.org/10.1002/2013GL059040.

——, and Coauthors, 2016: Advancing polar prediction capabilities on daily to seasonal time scales. *Bull. Amer. Meteor. Soc.*, **97**, 1631–1647, https://doi.org/10.1175/BAMS-D-14-00246.1.

King, J. C., T. Lachlan-Cope, R. S. Ladkin, and A. Weiss, 2008: Airborne measurements in the stable boundary layer over the Larsen Ice Shelf, Antarctica. *Bound.-Layer Meteor.*, **127**, 413–428, https://doi.org/10.1007/s10546-008-9271-4.

Kolstad, E. W., T. Breiteig, and A. A. Scaife, 2010: The association between stratospheric weak polar vortex events and cold air outbreaks in the Northern Hemisphere. *Quart. J. Roy. Meteor. Soc.*, **136**, 886–893, https://doi.org/10.1002/qj.620.

Kumer, V. M., J. Reuder, M. Dorninger, R. Zauner, and V. Grubišić, 2016: Turbulent kinetic energy estimates from profiling wind LiDAR measurements and their potential for wind energy applications. *Renew. Energy*, **99**, 898–910, https://doi.org/10.1016/j.renene.2016.07.014.

Lozier, M. S., and Coauthors, 2019: A sea change in our view of overturning in the subpolar North Atlantic. *Science*, **363**, 516–521, https://doi.org/10.1126/science.aau6592.

Manucharyan, G. E., and A. F. Thompson, 2017: Submesoscale sea ice-ocean interactions in marginal ice zones. *J. Geophys. Res. Oceans*, **122**, 9455–9475, https://doi.org/10.1002/2017JC012895.

Mauritzen, C., 1996: Production of dense overflow waters feeding the North Atlantic across the Greenland-Scotland Ridge. Part 1: Evidence for a revised circulation scheme. *Deep-Sea Res. I*, **43**, 769–806, https://doi.org/10.1016/0967-0637(96)00037-4.

Moore, G. W. K., I. A. Renfrew, and R. S. Pickart, 2012: Spatial distribution of air-sea heat fluxes over the sub-polar North Atlantic. *Geophys. Res. Lett.*, **39**, L18806, https://doi.org/10.1029/2012GL053097.

——, K. Våge, R. S. Pickart, and I. A. Renfrew, 2015: Decreasing intensity of open-ocean convection in the Greenland and Iceland seas. *Nat. Climate Change*, **5**, 877–882, https://doi.org/10.1038/nclimate2688.

——, A. Schweiger, J. Zhang, and M. Steele, 2018: What caused the remarkable February 2018 North Greenland polynya? *Geophys. Res. Lett.*, **45**, 13 342–13 350, https://doi.org/10.1029/2018GL080902.

Østerhus, S., and Coauthors, 2019: Arctic Mediterranean exchanges: A consistent volume budget and trends in transports from two decades of observations. *Ocean Sci.*, **15**, 379–399, https://doi.org/10.5194/os-15-379-2019.

Papritz, L., and T. Spengler, 2017: A Lagrangian climatology of wintertime cold air outbreaks in the Irminger and Nordic Seas and their role in shaping air–sea heat fluxes. *J. Climate*, **30**, 2717–2737, https://doi.org/10.1175/JCLI-D-16-0605.1.

——, and H. Sodemann, 2018: Characterizing the local and intense water cycle during a cold air outbreak in the Nordic Seas. *Mon. Wea. Rev.*, **146**, 3567–3588, https://doi.org/10.1175/MWR-D-18-0172.1.

Parkinson, C.L. and D.J. Cavalieri, 2008: Arctic sea ice variability and trends, 1979–2006. *J. Geophys. Res.*, **113**, C07003, https://doi.org/10.1029/2007JC004558.

Peng, G., W. N. Meier, D. J. Scott, and M. H. Savoie, 2013: A long-term and reproducible passive microwave sea ice concentration data record for climate studies and monitoring. *Earth Syst. Sci. Data*, **5**, 311–318, https://doi.org/10.5194/essd-5-311-2013.

Petersen, G. N., and I. A. Renfrew, 2009: Aircraft-based observations of air-sea fluxes over Denmark Strait and the Irminger Sea during high wind speed conditions. *Quart. J. Roy. Meteor. Soc.*, **135**, 2030–2045, https://doi.org/10.1002/qj.355.

Pickart, R. S., and M. A. Spall, 2007: Impact of Labrador Sea convection on the North Atlantic meridional overturning circulation. *J. Phys. Oceanogr.*, **37**, 2207–2227, https://doi.org/10.1175/JPO3178.1.

Pithan, F., and Coauthors, 2018: Role of air-mass transformations in exchange between the Arctic and mid-latitudes. *Nat. Geosci.*, **11**, 805–812, https://doi.org/10.1038/s41561-018-0234-1.

Rahmstorf, S., J. E. Box, G. Feulner, M. E. Mann, A. Robinson, S. Rutherford, and E. J. Schaffernicht, 2015: Exceptional twentieth-century slowdown in Atlantic Ocean overturning circulation. *Nat. Climate Change*, **5**, 475–480, https://doi.org/10.1038/nclimate2554.

Renfrew, I. A., G. N. Petersen, D. A. J. Sproson, G. W. K. Moore, H. Adiwidjaja, S. Zhang, and R. North, 2009: A comparison of aircraft-based surface-layer observations over Denmark Strait and the Irminger Sea with meteorological analyses and QuikSCAT winds. *Quart. J. Roy. Meteor. Soc.*, **135**, 2046–2066, https://doi.org/10.1002/qj.444.

——, A. D. Elvidge, J. Edwards, 2019: Atmospheric sensitivity to marginal-ice-zone drag: Local and global responses. *Quart. J. Roy. Meteor. Soc.*, **145**, 1165–1179. https://doi.org/10.1002/qj.3486.

Rogers, J. C., and M.-P. Hung, 2008: The Odden ice feature of the Greenland Sea and its association with atmospheric pressure, wind, and surface flux variability from reanalyses. *Geophys. Res. Lett.*, **35**, L08504, https://doi.org/10.1029/2007GL032938.

Semper, S., K. Våge, R. S. Pickart, H. Valdimarsson, D. J. Torres, and S. Jónsson, 2019: The emergence of the North Icelandic Jet and its evolution from northeast Iceland to Denmark Strait. J. Phys. Oceanogr., https://doi.org/10.1175/JPO-D-19-0088.1, in press.

Sévellec, F., A. V. Fedorov, and W. Liu, 2017: Arctic sea-ice decline weakens the Atlantic Meridional Overturning Circulation. *Nat. Climate Change*, **7**, 604–610, https://doi.org/10.1038/nclimate3353.

Sodemann, H., and Coauthors, 2017: The stable isotope composition of water vapour above Corsica during the HyMeX SOP1: Insight into vertical mixing processes from lower-tropospheric survey flights. *Atmos. Chem. Phys.*, **17**, 6125–6151, https://doi.org/10.5194/acp-17-6125-2017.

Spreen, G., L. Kaleschke, and G.Heygster, 2008: Sea ice remote sensing using AMSR-E 89 GHz channels. *J. Geophys. Res.*, **113**, C02S03, https://doi.org/10.1029/2005JC003384.

Strass, V. H., E. Fahrbach, U. Schauer, and L. Sellmann, 1993: Formation of Denmark Strait overflow water by mixing in the East Greenland Current. *J. Geophys. Res.* **98**, 6907–6919, https://doi.org/10.1029/92JC02732.

Swift, J. H., and K. Aagaard, 1981: Seasonal transitions and water mass formation in the Iceland and Greenland seas. *Deep-Sea Res.*, **28A**, 1107–1129, https://doi.org/10.1016/0198-0149(81)90050-9.

Tjernström, M., M. D. Shupe, I. M. Brooks, P. Achtert, J. Prytherch, and J. Sedlar, 2019: Arctic summer airmass transformation, surface inversions, and the surface energy budget. *J. Climate*, **32**, 769–789, https://doi.org/10.1175/JCLI-D-18-0216.1.

Våge, K., R. S. Pickart, M. A. Spall, H. Valdimarsson, S. Jónsson, D. J. Torres, S. Østerhus, and T. Eldevik, 2011: Significant role of the North Icelandic Jet in the formation of Denmark Strait overflow water. *Nat. Geosci.*, **4**, 723–727, https://doi.org/10.1038/ngeo1234.

——, ——, ——, G. W. K. Moore, H. Valdimarsson, D. J. Torres, S. Y. Erofeeva, and J. E. Ø. Nilsen, 2013: Revised circulation scheme north of the Denmark Strait. *Deep-Sea Res. I*, **79**, 20–39, https://doi.org/10.1016/j.dsr.2013.05.007.

——, G. W. K. Moore, S. Jónsson, and H. Valdimarsson, 2015: Water mass transformation in the Iceland Sea. *Deep-Sea Res. I*, **101**, 98–109, https://doi.org/10.1016/j.dsr.2015.04.001.

——, L. Papritz, L. Håvik, M. A. Spall, and G. W. K. Moore, 2018: Ocean convection linked to the recent ice edge retreat along east Greenland. *Nat. Commun.*, **9**, 1287, https://doi.org/10.1038/s41467-018-03468-6.

Vihma, T., and Coauthors, 2014: Advances in understanding and parameterization of small-scale physical processes in the marine Arctic climate system: A review. *Atmos. Chem. Phys.*, **14**, 9403–9450, https://doi.org/10.5194/acp-14-9403-2014.

Prepare for the Fall

with the perfect gifts for weather enthusiasts

Back to School Special -
10% discount*
Use code: Fall19
Coupon Valid until 10/31

Visit
www.ametsoc.org/amsbookstore
to learn more

*eligible products